Towards a better surface radiation budget analysis over sea ice in the high Arctic Ocean: a comparative study between satellite, reanalysis, and local-scale observations

Claudia Di Biagio, Jacques Pelon, Y. Blanchard, Lilian Loyer, Stephen R. Hudson, V. P. Walden, Jean-Christophe Raut, S. Kato, Vincent Mariage, Mats A. Granskog

To cite this version:

Claudia Di Biagio, Jacques Pelon, Y. Blanchard, Lilian Loyer, Stephen R. Hudson, et al.. Towards a better surface radiation budget analysis over sea ice in the high Arctic Ocean: a comparative study between satellite, reanalysis, and local-scale observations. Journal of Geophysical Research: Atmospheres, 2021, 126 (4), pp.e2020JD032555. 10.1029/2020JD032555 . insu-03040609

HAL Id: insu-03040609
https://insu.hal.science/insu-03040609

Submitted on 19 Mar 2021

JGR Atmospheres

RESEARCH ARTICLE
10.1029/2020JD032555

Toward a Better Surface Radiation Budget Analysis Over Sea Ice in the High Arctic Ocean: A Comparative Study Between Satellite, Reanalysis, and local-scale Observations

C. Di Biagio[1,2], J. Pelon[2], Y. Blanchard[3], L. Loyer[2], S. R. Hudson[4], V. P. Walden[5], J.-C. Raut[2], S. Kato[6], V. Mariage[2], and M. A. Granskog[4]

[1]LISA, UMR CNRS 7583, Université Paris-Est-Créteil, Université de Paris, Institut Pierre Simon Laplace (IPSL), Créteil, France, [2]LATMOS/IPSL, Sorbonne Université, Université Versailles Saint Quentin, CNRS, Paris, France, [3]Centre pour l'Étude et la Simulation Du Climat à l'Échelle Régionale (ESCER), Université Du Québec à Montréal, Montréal, Québec, Canada, [4]Norwegian Polar Institute, Fram Centre, Tromsø, Norway, [5]Department of Civil and Environmental Engineering, Washington State University, Pullman, WA, USA, [6]NASA Langley Research Center, Hampton, VA, USA

Key Points:

- Surface albedo, temperature, and cloud properties contribute to bias Clouds and the Earth's Radiant Energy System (CERES) and ERA-Interim surface irradiances, while ERA5 performs better
- In spring ERA-Interim and CERES SW and LW biases compensate allowing estimates of total surface radiation to agree with surface observations
- Differences up to 0.1 in gridded surface albedo remain between the datasets and affect shortwave and total surface radiation budgets

Supporting Information:

- Supporting Information S1

Correspondence to:
C. Di Biagio,
claudia.dibiagio@lisa.ipsl.fr

Citation:
Di Biagio, C., Pelon, J., Blanchard, Y., Loyer, L., Hudson, S. R., Walden, V. P. et al. (2021). Toward a better surface radiation budget analysis over sea ice in the high Arctic Ocean: a comparative study between satellite, reanalysis, and local-scale observations. *Journal of Geophysical Research: Atmospheres*, *126*, e2020JD032555. https://doi.org/10.1029/2020JD032555

Received 6 FEB 2020
Accepted 15 NOV 2020

Author Contributions:
Conceptualization: C. Di Biagio, J. Pelon
Data curation: S. R. Hudson, V. P. Walden, V. Mariage
Formal analysis: C. Di Biagio, J. Pelon, Y. Blanchard, L. Loyer, V. Mariage
Funding acquisition: J. Pelon, S. R. Hudson, V. P. Walden, M. A. Granskog
Investigation: S. R. Hudson, V. P. Walden, V. Mariage, M. A. Granskog
Methodology: C. Di Biagio, J. Pelon, Y. Blanchard, L. Loyer, S. R. Hudson, V. P. Walden, J.-C. Raut, M. A. Granskog
Project administration: J. Pelon, M. A. Granskog

Abstract Reanalysis datasets from atmospheric models and satellite products are often used for Arctic surface shortwave (SW) and longwave (LW) radiative budget analyses, but they suffer from limitations and require validation against local-scale observations. These are rare in the high Arctic, especially for longer periods that include seasonal transitions. In this study, radiation and meteorological observations acquired during the Norwegian Young Sea Ice Cruise (N-ICE2015) campaign over sea ice north of Svalbard (80–83°N, 5–25°E) from January–June 2015, cloud lidar observations from the Ice-Atmosphere-Ocean Observing System and the Cloud and Aerosol Lidar with Orthogonal Polarization are compared to daily and monthly satellite retrievals from the Clouds and the Earth's Radiant Energy System (CERES) and ERA-Interim and ERA5 reanalysis. Results indicate that surface temperature is a significant driver for winter LW radiation biases in both satellite and reanalysis data, along with cloud optical depth in CERES. In May, the SW and LW downwelling irradiances are close to observations and cloud properties are well captured (except for ERA-Interim), while SW upward irradiances are biased low due to surface albedo biases in all datasets. Net SW and LW radiation biases are comparable (~20–30 $\mathrm{W\,m^{-2}}$) but opposite in sign for ERA-Interim and CERES in May, which allows for error compensation. Biases reduce to ±10 $\mathrm{W\,m^{-2}}$ in ERA5. In June downward LW remains biased low (8–10 $\mathrm{W\,m^{-2}}$) in all datasets suggesting unsettled cloud representation issues. Surface albedo always differs by more than 0.1 between datasets, leading to significant SW and total flux differences.

1. Introduction

The Arctic is experiencing the fastest and most evident climate change on Earth (Serreze & Barry, 2011). Clouds and surface properties both play a crucial role in the surface energy budget of this region, as they determine the amount of shortwave (SW) and longwave (LW) radiation in the lower atmosphere. The water content in super-cooled boundary layer clouds is also of particular importance for the Arctic region (e.g., Pithan et al., 2018) as atmospheric circulation patterns may be changing (Graham et al., 2017b). The surface energy budget, in turn, affects sea ice growth and melt, evaporation, atmospheric structure, and stability, with consequences for regional and large-scale meteorology and climate (Bintanja & Krikken, 2016; Boucassa et al., 2013; Döscher et al., 2014). However, due to present day limitations in observations and atmospheric reanalysis, understanding and predicting climate change over this sensitive region still remains limited (Kay et al., 2016).

Both satellite and reanalysis products are often used for Arctic energy budget studies and aim to accurately represent cloud fraction, distribution and microphysical properties, as well as surface properties. However, it has been shown that both satellite-retrieved and model-simulated surface SW and LW radiation fields are largely biased in different seasons at high latitudes (Zygmuntowska et al., 2012; Kay & L'Ecuyer, 2013; Liu & Key, 2016; Lenaerts et al., 2017; Graham et al., 2017a, 2019). Biases in satellite products, such as the Clouds and the Earth's Radiant Energy System Energy Balanced and Filled (CERES-EBAF) as well as the Synoptic

Resources: J. Pelon, M. A. Granskog
Software: C. Di Biagio, Y. Blanchard, L. Loyer, V. Mariage
Supervision: J. Pelon, M. A. Granskog
Validation: C. Di Biagio
Visualization: C. Di Biagio
Writing – original draft: C. Di Biagio, J. Pelon
Writing – review & editing: C. Di Biagio, J. Pelon, Y. Blanchard, S. R. Hudson, V. P. Walden, J.-C. Raut, S. Kato, M. A. Granskog

TOA (Top-of-Atmosphere) and surface fluxes and clouds (CERES-SYN) products, appear to be quite significant in relation to cloud frozen water (CFW; Lenaerts et al., 2017). The fixed satellite overpass time and low spatial resolution may also contribute to biases in observations, but this problem is expected to be less critical in the Arctic, which experiences more frequent satellite overpasses than lower latitudes. Additionally, the assumptions made for retrieval algorithms (e.g., vertical cloud distribution) and/or the specification of surface albedo can be crude in terms of the regional and seasonal changes of ice and snow-covered surfaces in satellite products (e.g., Blanchard et al., 2014; Van Tricht et al., 2016). On the other hand, the ERA-Interim reanalysis dataset (Dee et al., 2011), that is, the global atmospheric reanalysis produced by the European Center for Medium-Range Weather Forecasts (ECMWF), has been shown to overestimate surface temperature and underestimate cloud liquid water (CLW) amount over the polar ocean in winter and spring (Graham et al., 2019; Lenaerts et al., 2017; Sedlar, 2018; Zygmuntowska et al., 2012) and, to a smaller extent, the CFW in similar conditions (Lenaerts et al., 2017). Recently the new ERA5 reanalysis was also produced by ECMWF, bringing several improvements in terms of resolution and overall quality, as for example, in sea surface temperature and sea ice parameters (Hersbach et al., 2019, 2020). Nevertheless, surface temperature bias (in winter) over sea ice still a concern in ERA5 (Wang et al., 2019).

The improvement of satellite and reanalysis products through a better representation of processes in meteorological models, is a primary objective of the A-Train space-borne observatory (https://atrain.nasa.gov/, Stephens et al., 2018). For example, the combination of such data has already been used to improve the parametrization of super-cooled boundary-layer water clouds at high latitudes (Forbes et al., 2016). Nonetheless, due to specific Arctic surface properties, improving satellite and reanalysis products requires having accurate surface-based field observations to compare with (Blanchard et al. 2014; Liu et al. 2017). Such observations are challenging and are mostly limited to the International Arctic Systems for Observing the Atmosphere coastal stations in the high Arctic (Uttal et al., 2016) and to a few sets of observations from dedicated field experiments and long-term stations over the Arctic region (e.g., Di Biagio et al., 2012). The first intensive field campaign documenting the cloud, albedo, and radiation fields and their coupled variations over a full-year period over the Arctic Ocean was the Surface HEat Budget of the Arctic (SHEBA) experiment, which occurred from October 1997 to October 1998 (Intrieri et al., 2002; Perovich et al., 2002; Persson et al., 2003; Shupe & Intrieri, 2004). Most of the campaigns following SHEBA were performed during summer when ship-based access is easiest (for example, the Arctic Sumer Cloud Ocean Study, ASCOS, [Tjenström et al., 2014], the Arctic Clouds in Summer Experiment, ACSE, [Sotiropoulou et al., 2016], and the measurements performed from the Tara vessel [Riihelä et al., 2017; Vihma et al., 2008]).

The Norwegian young sea Ice cruise (N-ICE2015, January–June 2015, http://www.npolar.no/en/projects/n-ice2015.html) is the most recent experiment to investigate processes linked to the younger and thinner Arctic sea ice during the winter to summer transition. Compared to SHEBA, N-ICE2015 was conducted in the more synoptically-active North Atlantic sector of the Arctic Ocean north of Svalbard. During N-ICE2015, observations of the atmosphere, ocean, ice dynamics, snow and ice physics, and marine ecosystem, including all components of surface SW and LW radiation and surface shortwave albedo, were performed (Granskog et al., 2018). Winter surface radiation data during N-ICE2015 showed a bimodal distribution of surface net (downward minus upward) LW flux comparable to that observed during SHEBA (Graham et al., 2017a). The two modes of the distribution correspond to clear-sky conditions (about -40 Wm^{-2}) and cloudy conditions ($\sim$0 Wm^{-2}) (Shupe & Intrieri, 2004). The radiatively clear state was shown to be usually prevalent during the Arctic winter (Stramler et al., 2011). Furthermore, satellite data indicate that the two winter states are likely to operate over the entire Arctic basin (Cesana et al., 2012; Stramler et al., 2011), but both large scale and regional models inadequately represent the atmospheric vertical stability and transitions between them (Pithan et al., 2016). The analyses performed by Graham et al. (2017a, 2019) for N-ICE2015 showed that positive biases of about +20 W m^{-2} (monthly averages) were linked to surface temperature biases in the ERA-Interim reanalysis with respect to ground-based observations.

During the N-ICE2015 field experiment, platforms from the Ice-Atmosphere-Arctic Ocean Observing System (IAOOS) project were deployed. The IAOOS network is the first ever ensemble of autonomous drifting buoys with both atmospheric and oceanic profiling instruments distributed over the high central Arctic, including the region north of 82°N (Provost et al., 2015). Other extensive programs of buoys deployment across the Arctic Ocean, such as the International Arctic Buoy Program (http://iabp.apl.washington.edu/index.html), were mostly focused on surface measurements over the past decades. Instead, the IAOOS buoys include a backscatter lidar system for cloud and aerosol profiling, surface meteorological sensors, snow and ice temperature profiler, and ocean profilers (Mariage et al., 2017; Provost et al., 2015). The IAOOS platforms were designed to perform regular year-round observations of the atmosphere, sea ice, and ocean composition and structure, simultaneously. IAOOS lidar observations acquired during the Barneo 2014 campaign (October–December 2014) and during N-ICE2015 (Di Biagio et al., 2018; Mariage et al., 2017) were used to investigate the occurrence and distribution of winter to summertime clouds and aerosols in the high Arctic Ocean. It was shown that low-level clouds (below 2 km altitude) were very frequent north of Svalbard in spring (Di Biagio et al., 2018). The observed attenuation of lidar signals confirms that mixed phase clouds occur often as previously reported from SHEBA observations (Shupe et al., 2006) and over Arctic land stations (Shupe, 2011).

In this study, the dataset of the radiation fluxes, surface albedo, meteorological parameters, and cloud occurrence and properties from N-ICE2015 and IAOOS in the winter to summer 2015 period were used in combination with Cloud and Aerosol Lidar with Orthogonal Polarization (CALIOP) space-borne data to compare with state-of-the-art satellite and reanalysis datasets: the CERES-SYN, CERES-EBAF, ERA-Interim and the new ERA5 products. The goal is to evaluate the accuracy of these data sets, which are widely used in Arctic research, with local-scale observations and identify sources of discrepancies. First, the data and analysis methods are presented in Section 2, followed by results of the comparisons in Section 3. The observed differences between the measurements and CERES-SYN and EBAF retrievals and ERA-Interim and ERA5 reanalysis are discussed with the aid of the IAOOS and CALIOP observations in Section 4 before concluding the study.

2. Data and Methods

In the following subsections, the different datasets used in this study and their processing, including spatial and temporal colocation, are described. Uncertainty estimates for all used variables and details on their calculation are provided in Table S1 in the supporting information.

2.1. Ground-Based Observations

2.1.1. N-ICE2015 Radiation, Albedo and Meteorological Data

Atmospheric measurements during N-ICE2015 were performed at an ice camp installed about 300 m away from the Norwegian research vessel Lance as it drifted with the sea ice from January–June 2015 north of Svalbard (Cohen et al., 2017; Granskog et al., 2018; Kayser et al., 2017; Walden et al., 2017). Meteorological conditions were highly variable in winter, with the passage of several storms, but became more stable in spring and summer (Cohen et al., 2017; Walden et al., 2017). The vessel was navigated into the ice pack, moored sequentially to four different ice floes and drifted with them (Cohen et al., 2017). The drift path for N-ICE2015 during this study period is shown in Figure 1 and covers the region ∼80°–83°N latitude and ∼5°–25°E longitude. The drifting periods were 38 days for Floe 1 (15 January–21 February), 24 days for Floe 2 (24 February–19 March), 49 days for Floe 3 (18 April–15 June), and 16 days for Floe 4 (7–21 June). A break was taken from mid-March to mid-April to refuel and resupply. The first three floes started in the northern part of the Nansen basin whereas Floe 4 drifted closer to the ice edge (see Figure 1 in Granskog et al. (2018) showing the ice extent on the May 25, 2015 and the N-ICE2015 floe trajectories).

Radiative fluxes at the surface were measured on all four floes during N-ICE2015 (Hudson et al., 2016; Walden et al., 2017). Downward and upward SW and LW irradiances (SW_{dw}, SW_{uw}, LW_{dw}, LW_{uw}) were measured at 1 min resolution by Kipp & Zonen CMP22 and CGR4 radiometers (200–3,600 nm and 4.5–42 μm bandwidth, respectively), both equipped with a Kipp & Zonen CVF4 heating and ventilation unit. Each of the radiometers was calibrated by the manufacturer before and after the field campaign. The accuracy was 2% (or 5 W m^{-2}) for global downward solar radiation, 3% for reflected solar radiation, and less than 3% for downward and upward longwave fluxes (Walden et al., 2017). The height of the instruments above the snow surface was between 1 and 1.2 m on each of the floes throughout the experiment. The surface below the instruments was snow, so that the field of view of the upward instruments was always a snow-covered sea-ice surface.

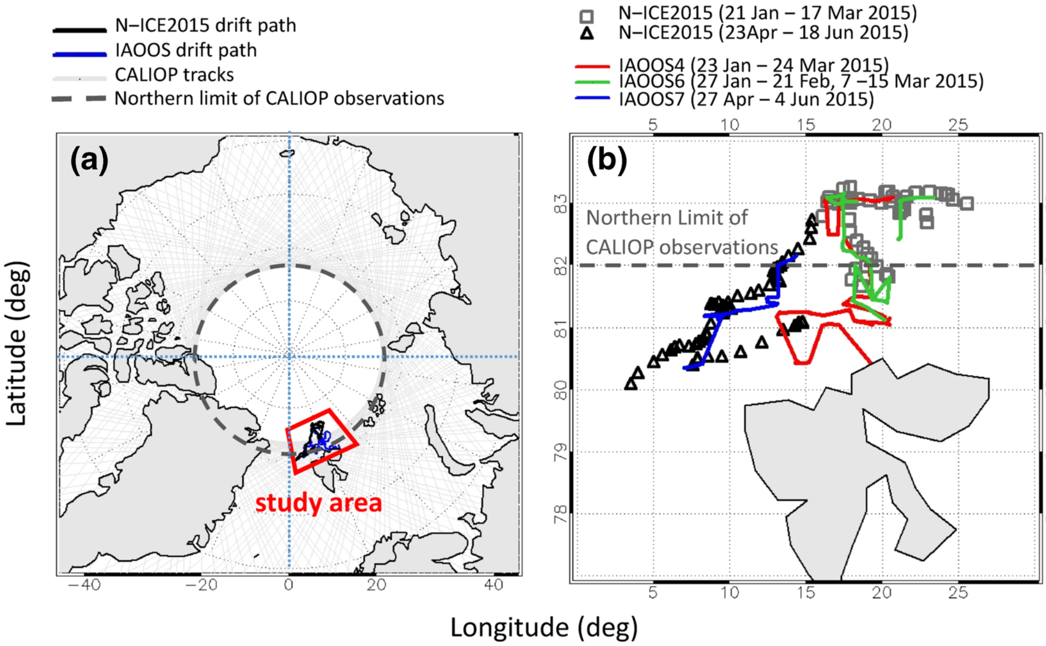

Figure 1. (a) Map showing the drift tracks of the N-ICE2015 ice camps and the three IAOOS buoys during the January–June 2015 period. The CALIOP tracks north of 70°N are also shown. The red area indicates the study area. (b) Detail of the N-ICE2015 and IAOOS drift paths in a smaller region north of Svalbard archipelago. The N-ICE2015 ship positions are shown as daily averages. CALIOP, Cloud and Aerosol Lidar with Orthogonal Polarization; IAOOS, Ice-Atmosphere-Arctic Ocean Observing System; N-ICE2015, Norwegian young sea ICE 2015.

The radiometers were checked daily to ensure that they were free of frost, rime, or moisture, and they were leveled and ventilated. A set of quality flags (QF) was developed for the data set (0-good data, 1-use with caution, and 2-bad data) (Walden et al., 2017). In our analysis, we considered only data with QF = 0 and eliminated days for which more than 30% of data had QF equal to 1 and 2. This removed 22 days of measurements, 12 of them in March, 2 in April, 4 in May, and 4 in June. Because of the need to reposition the ship when the floes broke up and the quality-control selection, the only almost complete month of radiation measurements was May (27 days). The other months have a fewer number of days of measurements: 11 (January), 19 (February), 4 (March), 6 (April), and 12 (June).

Surface broadband shortwave albedo (A) data, that is, the ratio of upward to downward SW irradiance measurements, were derived in springtime for a 3 h period centered around local noon (Walden et al., 2017).

Radiation instruments were installed close to the weather mast providing complementary meteorological data of temperature, pressure, wind speed and direction (Hudson et al., 2015). Meteorological radiosondes were launched twice a day (at about 0 UTC and 12 UTC), either from the ice by the ship or from the ship's deck (Hudson et al., 2017; Kayser et al., 2017).

2.1.2. IAOOS Lidar Observations of Aerosols and Clouds

Three IAOOS lidar systems, identified as IAOOS 4, 6, and 7, working at ~800 nm wavelength, were deployed in the region north of Svalbard during the N-ICE2015 campaign (see Figure 1). The IAOOS lidars profiled in the ~60 m–15 km altitude range. Measurements were performed up to four times per day with a typical 10-min averaging sequence for each profile and a vertical resolution between 15 and 60 m. Calibration and data corrections (desaturation, geometrical factor and background corrections) were performed to derive the attenuated backscatter coefficient (β_{att}) and the integrated attenuated backscatter (IAB) according to the analysis by Mariage et al. (2017). Clouds, aerosols, blowing snow, precipitation or pristine molecular profiles were discriminated using IAOOS observations with an algorithm based on lidar signal strength presented by Di Biagio et al. (2018). Near-surface (1.5 m) temperature and surface pressure were measured on these platforms.

The IAOOS low level (<2 km) cloud fraction was determined from observations as a 5-days running average of cloud occurrence measured by the lidar system (see also Di Biagio et al., 2018). The cloud optical thickness (COT) at 800 nm was estimated from IAOOS observations as follows. For large cloud backscattering (e.g., high cloud reflectance) the cloud transmission can be assumed to be very low so that the IAB is nearly constant and only depends on the lidar extinction-to-backscattering ratio S_c, and the multiple scattering factor η, as IAB = $1/(2\eta S_c)$ (Spinhirne et al., 1989). This allows the determination of the effective lidar extinction-to-backscattering ratio $S_{ce} = \eta S_c$. The backscattering coefficient (β) can then be derived from the attenuated backscattering coefficient by solving the lidar equation

$$\beta_{att}\left(z\right) = \beta\left(z\right)\exp\left(-2S_{ce}\int_0^z \beta\left(r\right)dr\right) \tag{1}$$

using a forward calculation algorithm (Klett, 1985). The extinction coefficient was retrieved as $\alpha\left(z\right) = S_c\beta\left(z\right)$, and the low cloud COT was equal to the product of the lidar ratio with the integrated backscatter coefficient: $COT = S_c\int_{z\min}^{z\max}\beta\left(r\right)dr$ for clouds from $z_{\min} = 0$ up to an altitude $z_{\max}$ considered here to be equal to 2 km. A multiple scattering factor $\eta = 0.8$, was considered here based on previous IAOOS lidar analyses (Mariage et al., 2017).

2.2. Satellite Observations

2.2.1. CALIOP Cloud Data

CALIOP data were considered in this study together with IAOOS surface observations to retrieve satellite information on cloud cover and vertical distribution (Winker et al., 2009). CALIOP is the primary instrument of the CALIPSO (Cloud-Aerosol Lidar and Infrared Pathfinder Satellite Observation) satellite. The CALIOP version 4.10 data products (Vaughan et al., 2017) were used. Data were available for the entire period of N-ICE2015. The cloud occurrence (%) for each day in the surrounding area of the N-ICE2015 measurement site was estimated as the ratio of the number of CALIPSO pixels with at least one cloud layer in the column to the total number of CALIPSO pixels in the region. The cloud occurrence was calculated for the whole 0–10 km altitude range and separately in the 0–2, 2–5, and 5–10 km altitude domains.

2.2.2. CERES-EBAF and CERES-SYN Radiation Data

Surface radiation data were derived from two CERES products: (i) the CERES-EBAF Surface Ed4.0 dataset (Kato et al., 2013) providing the monthly and climatological averages of surface clear-sky and all-sky upward and downward SW and LW fluxes and (ii) the SYN1deg-Day Edition 4.0 dataset (D. A. Rutan et al., 2015), hereafter referred as CERES-SYN, providing daily surface clear-sky and all-sky upward and downward SW and LW fluxes. Both datasets are over 1° by 1° global grid. In the retrieval algorithm, CERES TOA radiance measurements are converted into instantaneous SW and LW surface fluxes using scene-dependent angular directional models based on the Moderate Resolution Imaging Spectroradiometer (MODIS) retrievals of cloud properties and ancillary meteorological data from the Goddard Earth Observing System (GEOS) reanalysis product (version 5.4.1 in CERES-SYN).

The CERES-SYN surface irradiances are computed hourly by a radiative transfer model that uses as input MODIS-derived cloud properties (Collection 5). Temperature and humidity profiles used in computations are from GEOS data (Rienecker et al., 2008). The CERES-EBAF radiation product uses the CERES-SYN hourly irradiance as input, then data are adjusted and temporally interpolated to achieve consistency in the TOA fluxes with the CERES-SYN monthly mean (Kato et al., 2018). Uncertainties in the different components of the surface radiation fields are estimated in the Arctic as ± 14, ± 16, ± 12, and ± 12 $\mathrm{Wm^{-2}}$ for $\mathrm{SW_{dw}}$, $\mathrm{SW_{uw}}$, $\mathrm{LW_{dw}}$, and $\mathrm{LW_{uw}}$, respectively, for both the CERES-EBAF and CERES-SYN products (Kato et al., 2013, 2018). It should be noted that radiative fluxes derived from the combination of CloudSat, CALIPSO, and MODIS (2B-FLXHR-Lidar) are not yet available for the time period of this study. The daily and monthly surface broadband SW albedo was estimated in this study as the ratio between upward and downward all-sky CERES-SYN and CERES-EBAF shortwave irradiances. The broadband land surface albedos in both products are inferred from the clear-sky TOA albedo estimated from CERES measurements (Rutan et al., 2009). The MODIS data over partly cloudy scenes are used in the CERES retrievals to retrieve the surface albedo over the clear-sky portion of the partly cloudy scenes. The spectral surface albedo over ocean is based on look-up tables from Jin et al. (2004) and estimated as a function of solar zenith angle, wind speed, cloud and aerosol optical depth and ocean chlorophyll concentration. Over snow and ice, the spectrally-varying surface albedo is derived a function of grain size, solar zenith angle and optical depth (see CERES documentation at https://ceres.larc.nasa.gov/data/).

Cloud information for SYN data were also extracted. These are the cloud cover, the cloud visible (550 nm) COT, and the liquid and frozen cloud water content (CLW, CFW, units of kg m^{-2}) and are from the CERES-observed geostationary (GEO) and MODIS data products. For cloud cover we used the mid–high, mid–low, and low cloud types that are defined by their cloud-top height as being in the 500–300 hPa range (about 5.5–9 km height for a standard atmosphere of 288.15 K and 1013.25 hPa as surface temperature and pressure), 700–500 hPa range (3–5.5 km height) and greater than 700 hPa (below 3 km height), respectively. Note that only MODIS-derived cloud properties are used for surface irradiance computation over polar regions between 60° to poles because GEO data are only available between 60°S and 60°N. Also, it should be mentioned that the COT in SYN and EBAF is not the classical "1621" MODIS product, which is the best suited product for bright surfaces. This is because the Aqua–MODIS 1.6 μm channel used in the 1621 retrieval failed shortly after launch and the 1.24 μm channel was used as an alternative in both Aqua and Terra Ed4.0 daytime cloud optical depth retrievals over snow (Minnis et al., 2020). However, the 1.24 μm channel is not optimal for COT retrieval since more affected by surface reflectance. Surface shortwave downward flux validation of radiative transfer results over Dome C in Antarctica suggests that the 1.24 μm derived COT for thin clouds over snow can be overestimated by a factor of two or more (Loeb et al., 2018).

2.2.3. AMSR2 Sea Ice Concentration Data

Sea ice concentration (SIC) data, that is, the fraction of ocean covered by ice, were used as ancillary product to link point measurements of surface albedo and upward LW radiation during N-ICE2015 to gridded satellite observations and reanalysis products, as further discussed in Sect. 2.5. The SIC daily data were derived from AMSR2 (Advanced Microwave Scanning Radiometer 2) observations on the JAXA (Japan Aerospace Exploration Agency) satellite GCOM-W1 (Global Change Observation Mission 1st – Water). The Arctic Radiation and Turbulence Interaction STudy (ARTIST) Sea Ice algorithm (Spreen et al., 2008) is applied to microwave radiometer data to retrieve sea ice concentration data with a resolution of 6.25 and 3.125 km in latitude and longitude. The 3.125 km data were used here. The estimated error is 25% for 0% SIC and decreases to 5.7% at 100% SIC. For SIC above 65%, the error is less than 10% (Spreen et al., 2008).

2.3. Reanalysis Datasets: ERA-Interim and ERA5

The ERA-Interim reanalysis and forecast data (Dee et al., 2011) and the ERA5 dataset released in 2017 (Hersbach et al., 2020) were used in this study to compare meteorological, cloud properties and radiative fluxes to local scale observations. Data gridded at 0.25° latitude by 0.25° longitude were considered in the analysis. We used the 2-m air temperature (T2m), sea ice concentration (SIC), and low, middle, high, and total cloud cover (LCC, MCC, HCC, TCC, respectively), cloud liquid and frozen water content (CLW, CFW), and downward and upward LW and SW surface radiation fluxes for all-sky conditions. The LCC is for 800–1,000 hPa levels (about <2 km for standard atmosphere), middle cloud cover (MCC) 450–800 hPa (about 2–6 km), and high cloud cover (HCC) <450 hPa (about >6 km). For ERA-Interim the T2m, SIC, cloud cover, CLW and CFW data were from the reanalysis dataset while the surface radiation components were retrieved from the forecast dataset. The ERA-Interim reanalysis and forecast data were retrieved at their highest temporal resolution that is, 6 h for reanalysis data and 3 h for forecast data. The ERA5 dataset were available at 1 h resolution for all variables.

The CLW and CFW from reanalysis were used to estimate the COT at 550 nm for liquid and ice clouds using the formula by Mitchell (2002):

$$COT = \left(3Q_{\mathrm{ext}}CW\right) / \left(4\rho R_{\mathrm{eff}}\right) \tag{2}$$

The different terms in Equation 2 are the extinction efficiency (Q_{ext}), the water liquid or frozen content (CW), the density of water or ice (ρ), and the effective radius of the cloud particles (R_{eff}). For liquid clouds we assumed $Q_{\mathrm{ext}} = 2$, $\rho = 1{,}000$ kg m^{-3}, and $R_{\mathrm{eff}} = 10 \pm 5$ μm. For ice clouds we set $Q_{\mathrm{ext}} = 2.1$, $\rho = 916.17$ kg

m^{-3}, and $R_{eff} = 30 \pm 10$ μm. The Q_{ext} values were retrieved from Stengel et al. (2018), while the R_{eff} for liquid and ice clouds and their variability was taken from the literature (e.g., Han et al., 1994; King et al., 2004; Turner, 2005). To note that the R_{eff} is assumed fixed in Equation 2 for both water and ice clouds, while in reanalysis the R_{eff} is parameterized as a function of height for water clouds in ERA-Interim (R_{eff} varying between 10 μm at the surface and 45 μm at the top of the atmosphere) and following the Martin et al. (1994) parameterization in ERA5, and as a function of temperature for ice clouds (see the reanalysis documentation at https://www.ecmwf.int/en/elibrary/9233-part-iv-physical-processes and https://www.ecmwf.int/en/elibrary/16648-part-iv-physical-processes). Therefore Equation 2 is an approximation of the COT in ERA data.

The surface broadband albedo was estimated in this study as the ratio between SW_{uw} and SW_{dw} all-sky fluxes. In the ECMWF Integrated Forecasting System (IFS) the surface albedo is calculated considering separately solar radiation with wavelengths greater/less than 700 nm and for direct and diffuse solar radiation (giving 4 components to albedo). The land albedo for the four components are available at the start of the forecast and are calculated from a monthly climatology derived from MODIS not including the effects of snow. At each time step within the model, the four albedo components are updated to add the contribution from snow, represented as a single additional layer over the uppermost soil level and its albedo varies with snow age and depends on vegetation height. For low-vegetation conditions, snow albedo ranges between 0.52 (old snow) and 0.88 (fresh snow). The four albedo components are used as dynamic variables in the radiation scheme, and this implies that the amount of radiation reflected from the surface depends on cloud cover, trace gas concentrations, and solar zenith angle.

2.4. Radiative Transfer Modeling

Theoretical SW and LW upward and downward surface irradiances were determined with the radiative transfer code (RTC) Streamer version 3 (Key, 2002; Key & Schweiger, 1998), using surface and radiosonde meteorological observations performed from N-ICE2015 as input datasets (Hudson et al., 2015, 2017 https://data.npolar.no/dataset/). In the model, a discrete ordinate method is used to solve the radiative transfer equation. The RTC SW calculations were made every half-day for the latitudinal position of the surface camp and with reflectance values forced in each spectral band to match observations. Clear sky surface flux calculations were compared to N-ICE2015 surface radiation measurements for clearer periods (days 119 and 143) in high albedo conditions. An aerosol optical depth of about 0.005–0.012 was identified to make Streamer to match better with observations (agreement better than 10 W m^{-2} on SW fluxes). This is consistent with the average aerosol optical depth of 0.01 at 532 nm reported for the region by Di Biagio et al. (2018) based on CALIOP observations. Therefore, an aerosol-free atmosphere was considered in the calculations, which is expected to have a limited impact on both SW and LW calculations in cloudy conditions. The Streamer calculations were performed in the visible spectral domain at each day for different COT values assuming that a single 500 m thick layer of water cloud is present in the atmosphere. A best guess COT was estimated as the value providing the best agreement with the surface all-sky measured SW irradiances from N-ICE2015.

2.5. Spatial and Temporal Sampling of the Different Datasets

Satellite and reanalysis gridded datasets were extracted to be spatially co-located with the N-ICE2015 observations. To this aim, the CERES-SYN, ERA-Interim, ERA5, and AMSR2 provided at daily or sub-daily resolution and the monthly CERES-EBAF data were first selected and spatially averaged within ±0.5° latitude (±56 km) and ±0.5° longitude (±7–10 km at 83°–80°N) from the daily and monthly average N-ICE2015 positions, respectively. The ±0.5° condition was used in order to align to the CERES gridding resolution of 1°. This selection resulted in taking the CERES-SYN/EBAF closest grid cell to the N-ICE2015 average position for each day/month. Conversely, data in 16 cells (142–211 cells) around the N-ICE2015 position were averaged for ERA (AMSRS2) data based on the ±0.5° latitude/longitude selection. To test the sensitivity to spatial data sampling, we also extracted reanalysis data within ±0.25° latitude (±28 km) by ±0.25° longitude (±3–5 km) from the N-ICE2015 position. For ERA-Interim we found less than 3% difference (e.g., up to 10 Wm^{-2}) in the SW and LW irradiances and less than 2% in the surface albedo compared to extraction at 0.5° by 0.5°. As differences are both positive and negative, this can be considered as noise. This is, however, nonnegligible and should be kept in mind when interpreting the comparisons.

The CALIOP cloudiness data were also extracted to be co-located with the N-ICE2015 observations and were used to compare to the IAOOS, CERES, and ERA datasets. Given the limited number of overpasses per day from CALIOP over the N-ICE2015 study area, the ±0.5° latitude/longitude condition imposed for the other products did not allow retrievals of daily evolution of clouds at the local scale. The selection was thus extended to ±2° from the daily N-ICE2015 position. Average differences between 2% and 9% in the ERA cloud dataset (TCC, HCC, MCC, LCC) were obtained when extracting data within ±0.5° as compared to ±2°. These differences suggest that a direct comparison of ERA reanalysis data within ±0.5° from the N-ICE2015 position with CALIOP data within ±2° range is still meaningful. Smaller differences are expected for CERES data sampling over a larger grid (1° latitude/longitude).

The different datasets were then averaged daily and monthly for the comparisons. Monthly averages for ERA-Interim, ERA5, and CERES-SYN datasets were performed only over the days of N-ICE2015 measurements, to match observations. Even if these data are not complete monthly averages, they provide typical conditions for these months and allow a direct comparison with the N-ICE2015 observations. In contrast, these values provide only limited comparison to the CERES-EBAF monthly mean values, in particular for June when only 12 days of observations are available for N-ICE2015 in the first half of the month.

In order to compare N-ICE2015 local point measurements to satellite and reanalysis gridded data including both sea ice and open water fractions, we estimated the daily N-ICE2015-derived gridded surface albedo ($A_{\text{grid, N-ICE2015}}$) and upward LW irradiance ($\text{LW}_{\text{uw-grid,N-ICE2015}}$) as:

$$A_{\text{grid},N-\text{ICE2015}} = \left(\text{SIC}\cdot A_{N-\text{ICE2015}}\right) + \left(1-\text{SIC}\right)\cdot A_{\text{OCEAN}}\left(\theta\right) \tag{3}$$

$$LW_{\text{uw}-\text{grid},N-\text{ICE2015}} = \left(\text{SIC}\cdot\sigma\cdot\varepsilon_{\text{SNOW}-\text{ICE}}\cdot T^{4}_{N-\text{ICE2015}}\right) + \left(1-\text{SIC}\right)\cdot\varepsilon_{\text{OCEAN}}\cdot\sigma\cdot\left(273.15-1.8\right)^{4} \tag{4}$$

The SIC in Equations 3 and 4 was taken from daily AMSR2 observations extracted around N-ICE2015 position, and $\sigma = 5.67\ 10^{-8}\ \text{J s}^{-1}\ \text{m}^{-2}\ \text{K}^{-4}$ is the Stefan-Boltzmann constant. In Equation 3, we calculated the daily mean open water albedo A_{OCEAN} as a function of the solar zenith angle (θ) following the formulation of Taylor et al. (1996). For the range of daily averaged θ at the N-ICE2015 position (between 67° and 80° in the April to June period) the A_{OCEAN} albedo varies between 0.06 and 0.15. In Equation 4 we assume that the open water temperature is that of the freezing point of sea water (−1.8°C) and that the emissivity of snow-ice and ocean is 1. As shown in Feldman et al. (2014) the emissivity of snow-ice and ocean is however lower than 1 and varying with wavelength, with average values of 0.975 for snow-ice and 0.925 for ocean over the thermal infrared domain. We also assume in Equation 4 that the $T_{N\text{-ICE2015}}$ measured at 2 m height equals the surface skin temperature. The comparison with the CERES-SYN data shows that $T_{N\text{-ICE2015}}$ is within 4% the gridded T_{skin} from satellite. The approximations in Equation 4 as well as the uncertainty on SIC and $A_{N\text{-ICE2015}}$ were taken into account to estimate the overall uncertainty on $A_{\text{grid},N\text{-ICE2015}}$ and $\text{LW}_{\text{uw-grid},N\text{-ICE2015}}$ (see Table S1). The surface albedo and the upward SW irradiance are the two quantities most influenced by the open water fraction, therefore showing possible differences passing from local to grid spatial scales. The upward LW is less affected in spring as temperature and emissivity of ice and water are similar. Equations 3 and 4 would allow a quantitative evaluation of the impact of the open water area in the grid cell for these two variables. This will be discussed in Section 3.1.2.

2.6. Uncertainty Calculation and the Impact of Spatial Sampling

Table S1 in the supporting information summarizes data, uncertainties and their method of calculation as considered in the present analysis. The uncertainty of daily and monthly averages is the associated standard deviation, while the error propagation formula is used to estimate the uncertainty for derived quantities. For CERES-SYN and EBAF we assume nominal uncertainties on radiation products from the literature (Kato et al., 2013, 2018). For reanalysis, CALIOP and AMRS2 data together with daily and monthly average, data are also spatially aggregated to represent an average ± 0.5° area around N-ICE2015. The uncertainty (standard deviation) on the spatial averaging is not taken into account in the present analysis, with the only exception of SIC from AMSR2. For reanalysis data the standard deviation over temporal averaging is usually much larger than the one derived from spatial averaging (for instance it is less than 1%–2% for T2m and LW radiation components) or of the same order of magnitude but related mostly to random spatial fluctuations

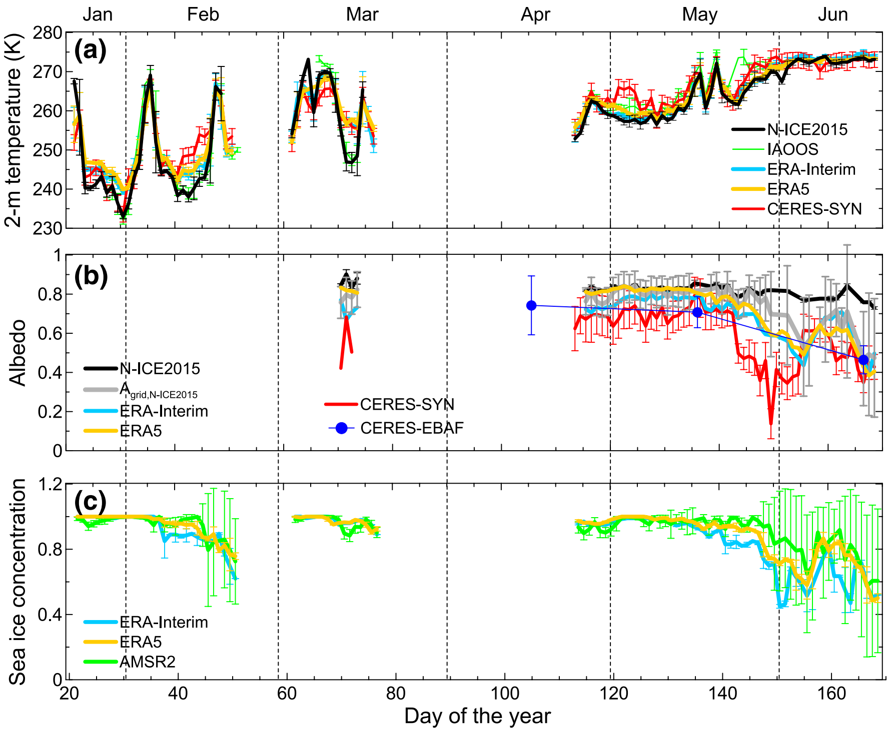

Figure 2. (a) Near surface temperature from 2 m sensor on the meteorological mast during N-ICE2015, *T*2m from the ERA-Interim and ERA5 reanalysis datasets, and from the IAOOS T1.5 m sensors. The skin temperature from CERES-SYN is also shown. Data are daily averages ± their standard deviation. (b) Daily average surface shortwave all-sky broadband albedo from N-ICE2015, ERA-Interim, ERA5, and CERES-SYN datasets and monthly mean albedo from CERES-EBAF. The N-ICE2015 gridded data represent the observed data for the grid cell of 0.5° by 0.5° latitude and longitude around N-ICE2015 position calculated from Equation 3. For the sake of clarity, only the uncertainty on N-ICE2015 point and gridded data and CERES-EBAF and CERES-SYN datasets are shown while uncertainties on reanalysis data are omitted. (c) Daily average ± standard deviation of sea ice concentration from ERA-Interim and ERA5 reanalysis datasets, and retrieved from AMSR2 satellite observations. Data from ERA-Interim, ERA5, CERES-SYN, and AMSR2 are within ±0.5° latitude and longitude from daily N-ICE2015 average positions. The CERES-EBAF data are extracted within ±0.5° latitude and longitude from monthly N-ICE2015 average positions. CERES, Clouds and the Earth's Radiant Energy System; ASMR2, Advanced Microwave Scanning Radiometer 2; ERA, ECMWF reanalysis; IAOOS, Ice-Atmosphere-Arctic Ocean Observing System; N-ICE2015, Norwegian young sea ICE 2015.

in particular for cloud cover and CLW and CFW variables. For variables affected by spatial heterogeneity, as the SIC, surface albedo and SW radiation components affected by sea ice melting and dynamics during spring and summer, the spatial distribution of data and its impact on averaging is discussed in the next sections and supported by histograms in the main text and in the supporting information.

3. Results

3.1. Meteorological and Surface Properties Data

3.1.1. Surface Temperature

Near surface temperature measurements during N-ICE2015 observed both close to the ship and by the IAOOS buoys are shown in Figure 2a. Field data show that the evolution of the 2 m temperature is strongly modulated by large-scale storm events entering from the North Atlantic (Cohen et al., 2017). The near-surface temperature typically varies between a cold state (230–240 K) and a warm state (~270 K) in January and February. In springtime, the temperature gradually increases to reach a rather stable 270–275 K in June. The temperature datasets from IAOOS and N-ICE2015 agree on average better than 0.5 K (±0.8 K) in wintertime, but the IAOOS measurements are on average higher by about 2.5 K in springtime, possibly due to solar heating of the body of the buoy; one exception is the large peak difference that exceeds 10 K that was observed on day 144. Some of these differences may be also explained by the distance between the buoy and the ship in spring. As shown in Graham et al. (2019) and Wang et al. (2019), and evident in Figure 2a, ERA-Interim and ERA5 have a positive temperature bias of 2–11 K during clear, cold periods in January and February (days 20–60). Whereas, there is an excellent agreement with the observations during winter for cloudy periods and throughout spring (although there can be a 2–4 K bias in some cases). The CERES-SYN temperature has a positive bias during winter clear periods (differences up to 11 K) while it is in good agreement during springtime with few exceptions in early May (differences up to 7 K).

3.1.2. Surface Broadband Albedo

The surface broadband albedo (Figure 2b) derived from N-ICE2015 SW fluxes (Walden et al., 2017) shows relatively constant and high values (~0.82) for snow covered sea ice in early spring weakly decreasing during spring, suggesting that no significant changes in surface state occurred locally along the N-ICE2015 drift path before mid-June. It is to be noted that albedo values observed in April during N-ICE2015 were only slightly smaller than those observed for thicker ice in 1998 during SHEBA (Perovich et al., 2002). However, the sea ice in the Svalbard region was very dynamic, and there were often open water leads in the vicinity of the ice camp. When looking at the gridded N-ICE2015 albedo retrieved from Equation 3 it appears evident that two periods exist: the first one before day 145 (May 25th) when point and gridded albedo agree because SIC is close to 100%. This is corroborated by histograms shown in Figure S1 in the supporting information indicating a monomodal distribution peaked between 90% and 95% for SIC for AMSR2 and also for ERA data over the whole analyzed region around N-ICE2015 position for two periods before day 145. In this phase, the point albedo measurements from N-ICE2015 are representative of the grid cell albedo. The second period after day 145 shows a significant discrepancy (up to 0.2) between point and gridded albedo because of the melt onset in late May and the decrease of the SIC over the studied area (Figure 2c). Figure S1 shows that after day 145 the spatial distribution of the SIC becomes more heterogeneous and shows in late spring values spanning from <10% to >95% in AMSR2, therefore representative of ice-covered and ice-free regions. This will impact SW_{uw} irradiance comparisons. We note that point (N-ICE2015) and gridded (satellite, reanalysis) SW fluxes will not be directly comparable after day 145. On the opposite, we have determined from Equation 4 that the LW_{uw} irradiance differs less than 5% between point and gridded definitions in winter and early spring and less than 2% during May and June, since ice and water surface temperatures are similar. Thus, for LW_{uw} we can assume point values to be representative of the grid cell for comparison with satellite and reanalysis datasets throughout the whole investigated period. The histograms identifying average values and time distributions will be discussed in more detail in Section 3.2.

Compared to N-ICE2015 observations, both ERA-Interim and ERA5 surface albedo data are in agreement with both point and gridded data before and after day 145 within uncertainties, despite an underestimation of 0.05–0.1 in ERA-Interim compared to point observations. After day 145 both ERA products underestimate by up to about 0.1 the N-ICE2015 gridded albedo and by up to 0.25 the point measurements. In reanalysis data the mid-May to mid-June period corresponds to a strong decrease in sea ice cover as shown in AMSR2 data. The SIC decrease is larger in ERA-Interim and ERA5 than observed with AMSR2 (Figure 2c) between days 145 and 155 in particular, which could explain the lower bias compared to the N-ICE2015 gridded albedo in this period. The sea ice concentration continues to be lower in ERA-Interim compared to AMSR2 in mid-June, but not in ERA5, nonetheless the surface albedo is in good agreement (less than 0.1 difference) with N-ICE2015 gridded data for both ERA-Interim and ERA5. Examples of the spatial distribution of surface broadband SW albedo for ERA-Interim and ERA5 is provided in Figure S2.

The CERES-SYN product underestimates the surface albedo by 0.1–0.3 compared to N-ICE2015 point measurements, with peaks of 0.6 difference in end of May (day 150). Differences are lower but still significant (larger than 0.1 and up to 0.3–0.4) when comparing to N-ICE2015 gridded data. The CERES-EBAF dataset is comparable to CERES-SYN. It is to be noted that CERES, ERA-Interim, and ERA5 values agree to within 0.1–0.2 until mid-May (day 140) and in mid-June and diverge in between.

The underestimation of the seasonal CERES albedo dataset compared to local observations was already reported for spring by Pistone et al. (2014) and Riihelä et al. (2017). Part of the difference, as also seen in comparison to the N-ICE2015 gridded data in Figure 2b, may be explained by considering the different spatial resolution of the different products and the N-ICE2015 observations. As reported in Itkin et al. (2017), the distance to the sea ice edge was between 50 and 250 km for most of the N-ICE2015 experiment. This distance is not very large compared to the size of the grid of ERA-Interim (0.25° by 0.25°) or more particularly for CERES (1° by 8° between 80° and 89° latitude, Doelling et al., 2013). Significant differences may be expected especially for CERES when the ship is close to the ice edge (end of March, April and May). After repositioning the ship to the north at the end of April, the distance to the ice edge is larger and the differences in albedo are smaller (but still about 0.1–0.2 both compared to point and gridded data).

In conclusion, this analysis shows that albedo is a critical parameter to determine, but beyond scale issues, it seems that both ERA-Interim and more particularly CERES are underestimating its value for early spring when the spatial distribution of sea ice is quite homogeneous around the ship position. This suggests that problems exist in the representation of surface state and properties in these products independently of the spatial sampling differences compared to surface observations. Conversely, ERA5 works better in representing albedo in particular in early spring period. It should be also noted that albedo measurements derived around noon during N-ICE2015 are only lower limit estimates of the real daily albedo, that is surface snow albedo increases for increasing solar zenith angles (Wiscombe & Warren, 1980). Therefore, differences between CERES/ERA-Interim/ERA5 and N-ICE2015 should be expected to be even larger than reported here because of the different temporal sampling.

3.1.3. Cloud Occurrence, Structure, and Properties

The IAOOS lidar observations show a high occurrence of clouds (Figures 3a and 3b), in particular between days 30 and 40 (early February) that are associated with storm events seen in Figure 2a. More stable meteorological conditions were reached during spring, with a persistent layer of low-level clouds. These were mostly water clouds as characterized by strong backscattering and attenuation (Di Biagio et al., 2018) observed by IAOOS during May (days 120–150). The dominance of low-level clouds in spring in this region is confirmed by CALIOP observations (Figure 3b); in this dataset, clouds below 2 km represent between 40% and 100% of the total cloud cover between days 120 and 170. Examining the CALIOP observations at larger scales (not shown) suggests that low-level clouds in spring occur frequently over the entire Arctic Ocean, which may be linked to Bering and Siberian air inflows (Di Biagio et al., 2018).

Figure 3 also shows that some differences exist between the IAOOS and CALIOP cloud observations, particularly in winter. This is probably due to the different temporal and spatial sampling between the two datasets: IAOOS are local scale observations over 10-min averages every 4 h, whereas CALIOP data are averages over ±2° around the IAOOS position over several overpasses that are hours apart. Moreover, the IAOOS lidar is looking from the surface, not detecting clouds above low clouds when they are present (mostly water clouds in spring as previously mentioned). Whereas, CALIOP measures the entire troposphere using observations from the top of the atmosphere, with exception of some low-level clouds (Blanchard et al., 2014).

Compared to CALIOP observations, both ERA-Interim and ERA5 generally overestimates cloud cover at all levels during wintertime over the study region (Figures 3c–3f). This difference in cloud cover was already identified in previous studies over the Arctic Ocean (Zygmuntowska et al., 2012), and in particular during storm periods. On the contrary, both reanalysis products perform well at reproducing the occurrence of medium and high clouds compared to CALIOP during spring, as well as the dominance of LCC during this period, which is present in both the CALIOP and IAOOS datasets. Nonetheless, the exact amount and temporal variations of cloud cover at all levels is somewhat different in ERA-Interim and ERA5 compared to CALIOP and IAOOS, with periods of both underestimation and overestimation of LCC and/or TCC in ERA-Interim and a general overestimation of LCC in ERA5. In particular, it is seen that during May, although good agreement in low cloud cover is observed, most of the time the associated COT remains smaller in ERA-Interim (see Figures 4a and 4b). Indeed, only the mid-May (days 135–142) and June periods show significant liquid water content and higher COT in ERA-Interim (see Figure 4c). Examples of the distribution of the ERA-Interim and ERA5 COT over the analyzed region in three different periods in spring are shown in Figure S3. It is interesting to note from Figure 3 that the TCC is always larger than 50% for reanalysis products, including non-negligible amount of both low and high clouds, also during the clear periods identified in the temperature dataset in Figure 2a in January and February. The COT is however about zero during the winter clear periods in both ERA-Interim and ERA5 and associated to almost zero water, suggesting that very thin clouds contribute to the cloud cover in these periods.

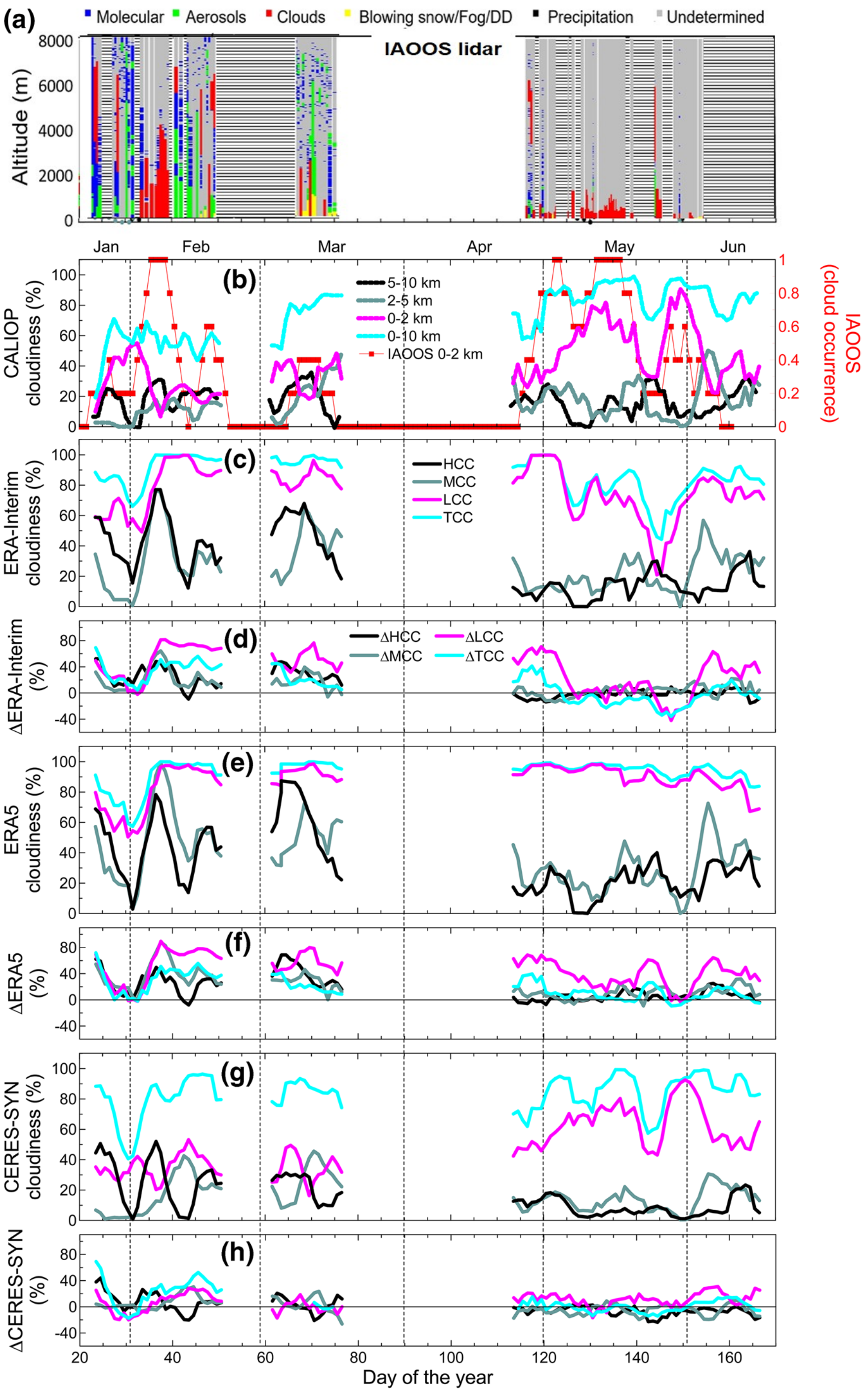

Figure 3. (a) Vertical cross section of the feature classification from IAOOS lidar observations co-located with N-ICE2015 observations (DD indicates Diamond Dust; white regions correspond to periods with no measurements, while gray parts stands for altitudes where the lidar signal was not exploitable); (b, c, e, and g) vertically resolved cloud occurrence obtained from CALIOP measurements, ERA-Interim and ERA5 reanalysis datasets, and CERES-SYN (from MODIS algorithm), respectively, in the period from January–June 2015 north of Svalbard. For CERES-SYN cloud HCC correspond to the mid-high clouds, MCC to the mid-low clouds, and LCC to the low clouds classes. Five day running average of IAOOS low clouds (<2 km) occurrence is also shown in panel (b). Panels (d, f, and h) report the differences in cloud occurrence between ERA-Interim, ERA5, CERES-SYN, and CALIOP, respectively. The ΔHCC is (HCC—CALIOP 5–10 km), ΔMCC is (MCC—CALIOP 2–5 km), ΔLCC is (LCC—CALIOP 0–2 km), and ΔTCC is (TCC—CALIOP 0–10 km). The ERA-Interim, ERA5, and CERES-SYN data are within ±0.5° lat/lon from daily N-ICE2015 average position whereas CALIOP is within ±2.0°. Data are shown as 5-days running averages in all plots with the exception of the IAOOS profiles in (a) that are measured at 10-min intervals. CALIOP, Cloud and Aerosol Lidar with Orthogonal Polarization; CERES, Clouds and the Earth's Radiant Energy System; ERA, ECMWF reanalysis; HCC, high cloud cover; IAOOS, Ice-Atmosphere-Arctic Ocean Observing System; LCC, low cloud cover; MCC, middle cloud cover; TCC, total cloud cover.

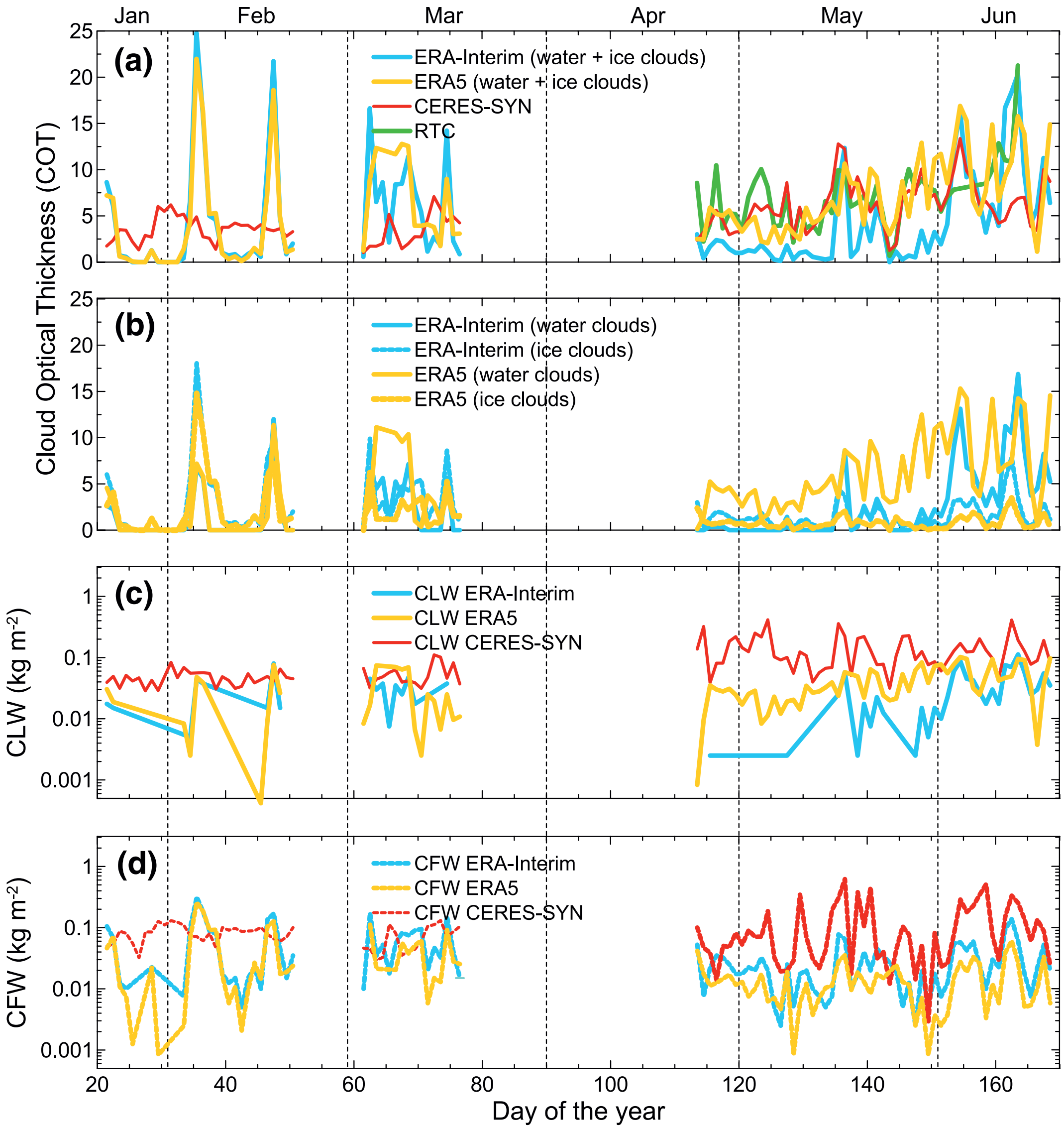

Figure 4. (a) Visible cloud Optical thickness (COT) from ERA-Interim, ERA5, and CERES-SYN and the COT from the radiative transfer code (RTC). (b) COT for liquid and ice clouds, (c) cloud liquid, and (d) cloud frozen water content (CLW, CFW) for ERA-Interim, ERA5, and CERES-SYN. Data are shown as daily averages. The COT for ERA-Interim and ERA5 is retrieved from Equation 2 assuming a fixed R_{eff} for clouds. CERES, Clouds and the Earth's Radiant Energy System;ERA, ECMWF reanalysis.

The CERES-SYN product reproduces the cloud occurrence very well and the repartitioning of low, medium, and high clouds as compared to CALIOP data in the spring to summer time (Figures 3g–3h). However, an overestimation of cloud occurrence at all levels (as well as COT in clear periods) is detected in wintertime compared to CALIOP observations, but a lower cloud cover is usually found compared to reanalysis. Note that the cloud levels are not exactly the same between the different products, and this may lead to some discrepancy. It should be mentioned that previous works have indicated underestimation of CERES cloud occurrence in the Arctic linked with the dominance of thin clouds in this region and the relative high COT threshold values in MODIS cloud mask algorithms (e.g., COT of 0.5 for the MODIS 1621 product for bright surfaces for instance leading to 22% undetected clouds in the Arctic, Chen et al., 2019). This underestimation is not apparent in our dataset compared to CALIOP observations.

As shown in Figure 4c, the CLW and CFW is significantly higher in CERES compared to ERA-Interim, leading to a COT larger than five for CERES most of the time in spring, and much smaller values (frequently

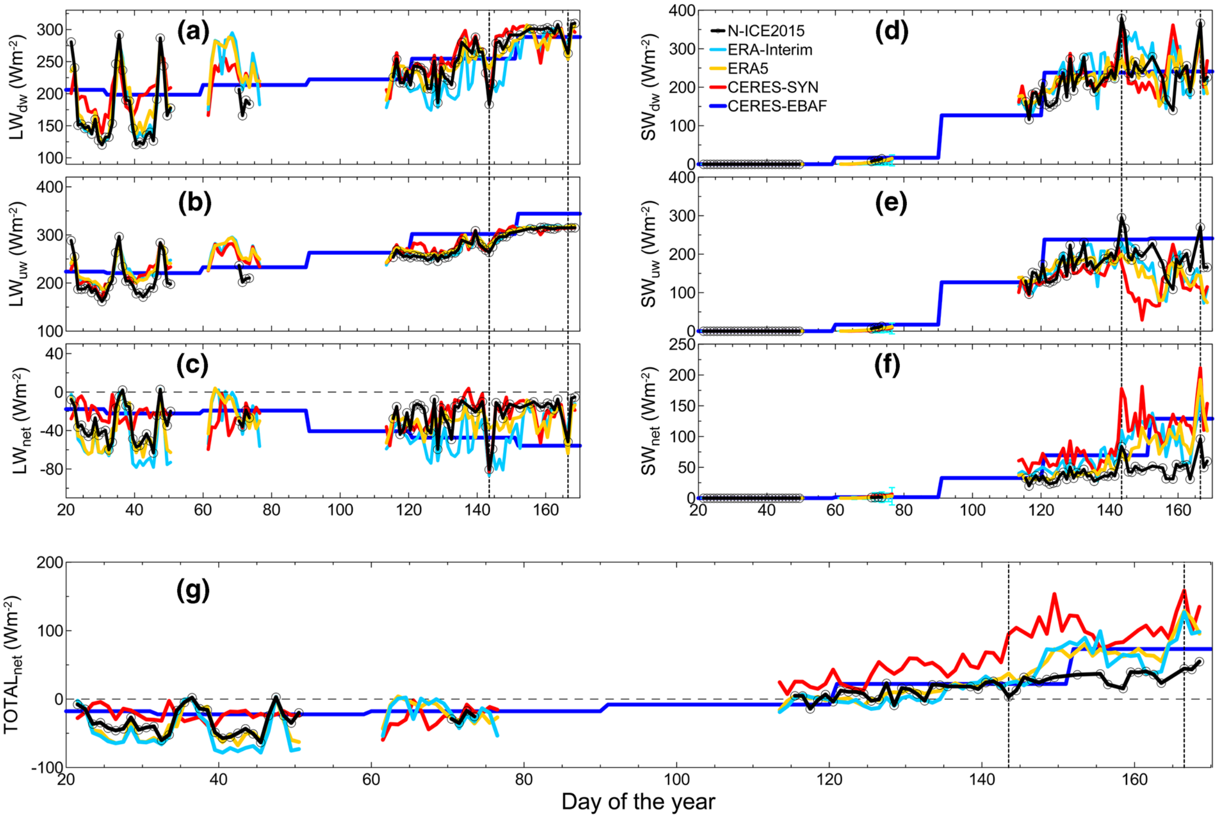

Figure 5. (a–f) Temporal evolution of SW and LW downward (dw), upward (uw), and net (dw-uw) irradiance data and (g) total (SW + LW) net irradiance for N-ICE2015 and co-located ERA-Interim, ERA5, CERES-SYN, and CERES-EBAF datasets. All data are shown as daily averages except CERES-EBAF data that are monthly averages. For the sake of clarity error bars are not shown in the plots. Clear sky episodes (days 143 and 166) are marked by vertical dotted lines. Data interruptions occurred in different periods due to N-ICE2015 measurement gaps or due to data quality. CERES, Clouds and the Earth's Radiant Energy System; ERA, ECMWF reanalysis; LW, longwave; N-ICE2015, Norwegian young sea ICE cruise; SW, shortwave.

below 1) for ERA-Interim. The CLW and CFW for CERES on the contrary are at about 0.5 and 1 kg m^{-2} almost constantly during winter (as well as the COT), therefore they do not reproduce the alternation of clear and storm periods as instead reproduced in ERA data as the combination of liquid and ice clouds. This results, as previously noted, in an overestimate of the COT in clear periods and an underestimate during storm periods in winter in the CERES dataset. The COT from CERES for April and May is in good agreement with the COT retrieved from the N-ICE2015 radiation measurements using the radiative transfer code simulations. The ERA5 dataset shows larger CLW compared to ERA-Interim (up to 5 times higher) in particular during spring leading to considerably higher COT values than ERA-Interim, values that are in good agreement with CERES and RTC estimates. However, it is interesting to note that the COT agrees between ERA5 and CERES in many times in spring even if the corresponding CLW and CFW are significantly higher in CERES data, suggesting different assumptions in MODIS retrieval compared to Equation 2 used here for ERA COT retrieval. Average values of about 5 are seen in early May (days 124–134) and at the end of May (146–151) but are close to 10 for days 135–142. Average values in June are in better agreement with the total optical depths from ERA-Interim over the atmospheric column, although CERES exhibits smaller values near day 163. The clear-sky episodes on days 143 and 166 are well identified, despite a COT between 1 and 5 is obtained.

3.2. Radiative Fluxes

Radiative fluxes measured during N-ICE2015 (Walden et al., 2017) and those from CERES-SYN, CERES-EBAF, ERA-Interim and ERA5 are shown in Figure 5. Differences between N-ICE2015 observations and reanalysis/satellite data are illustrated in Figure 6.

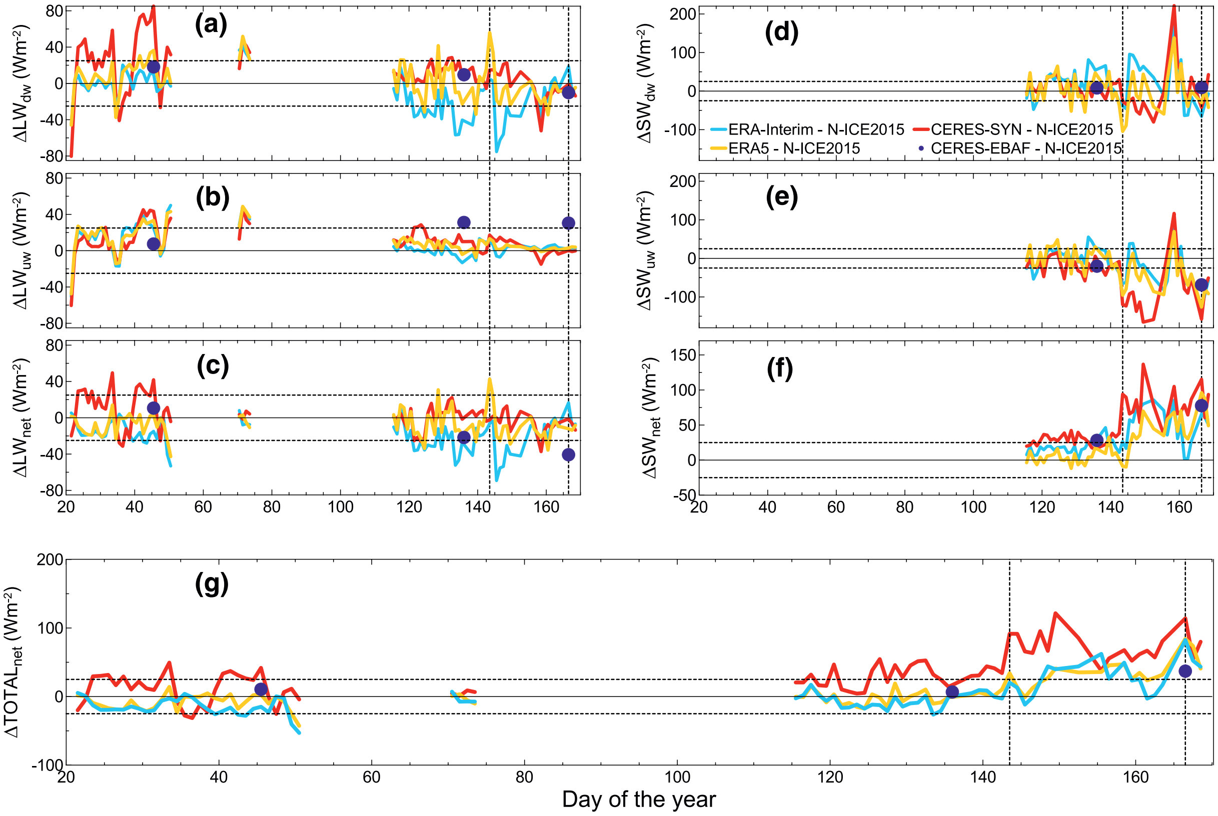

Figure 6. Differences between ERA-Interim, ERA5, and CERES-SYN daily and CERES-EBAF monthly LW, SW, and net radiation data from N-ICE2015 observations. Horizontal dotted lines represent constant values of ±25 $\mathrm{Wm^{-2}}$. CERES, Clouds and the Earth's Radiant Energy System; ERA, ECMWF reanalysis; LW, longwave; N-ICE2015, Norwegian young sea ICE cruise; SW, shortwave.

3.2.1. Winter Longwave Radiation

In winter, as discussed by Graham et al. (2017a) and Walden et al. (2017), and in agreement with earlier SHEBA data (Shupe & Intrieri, 2004; Stramler et al., 2011), longwave radiation switches between two states: one with a near neutral LW net budget ($\mathrm{LW_{net}}$ ~0 $\mathrm{Wm^{-2}}$) namely the "opaquely cloudy state" (storm periods), and another with a large negative (upward) net longwave radiative flux $\mathrm{LW_{net}}$ of −40 to −60 $\mathrm{Wm^{-2}}$ namely the "radiatively clear state." These two states correspond to the warm and cold winter temperature cases shown in Figure 2a. As described by Graham et al. (2019), ERA-Interim and ERA5 capture the "opaquely cloudy" and the "radiatively clear" states and their transition during N-ICE2015, as shown in LW fields (Figures 5a–5c). However, clear states are associated with a high positive surface temperature bias, resulting in an overestimation of $\mathrm{LW_{uw}}$. A negative bias is observed for both $\mathrm{LW_{uw}}$ and $\mathrm{LW_{dw}}$ radiation components during the "opaquely cloudy" storm periods, possibly due to the fact that the enhanced cloudiness compared to observations (Figures 3c–3d), is not capable to fully compensate for lower CLW and CFW in the ERA-Interim as previously identified (Lenaerts et al., 2017). The ERA5 $\mathrm{LW_{dw}}$ dataset is also biased high in clear sky period in early February (Graham et al., 2019). As a result, the total net radiation in winter from ERA-Interim and ERA5 is in agreement with N-ICE2015 during storms and periods of high cloudiness. However, the net radiation is significantly underestimated during clear periods in particular for ERA-Interim, leading to a net surface cooling from that is, about 25–30 W $\mathrm{m^{-2}}$ larger than the observations on daily time scales. The negative bias is lower for ERA5, but particularly in early February this reflects a larger compensation of downward and upward LW biases.

The CERES-SYN data reproduce the transition between clear and cloudy periods in winter in $\mathrm{LW_{dw}}$ and $\mathrm{LW_{uw}}$ data, but both components are positively biased during clear phases due to the temperature bias and the overestimate of COT during clear-sky periods in the CERES product (Figure 4a). The $\mathrm{LW_{dw}}$ is also strongly biased low (down to 40 W $\mathrm{m^{-2}}$) during storm periods because of the underestimation of COT as shown in Figure 4a. As a consequence, the winter transition between clear and cloudy periods is marked by a shift from positive bias up to about 40 W m^{-2} during clear periods to negative bias down to 30 W m^{-2} during storm phases in the LW_{net} radiation.

3.2.2. Spring Longwave and Shortwave Radiation

The situation changes in spring when cloudiness is dominated by low clouds and local scale forcings as SW radiation is now contributing significantly to the radiative budget. Also, the surface albedo changes as snow melt begins, which affects SW radiation. During spring, there were two short episodes of clear skies on days 143 and 166, corresponding to local minima of net LW radiation. The second episode is outside of the period of IAOOS observations, but the first one corresponds to a transition between low-level dense water clouds to mid-level extended ice clouds (Figure 3b). This decrease is also seen in the larger-scale cloud fractions from CALIOP, ERA-Interim and CERES-SYN data (Figures 3b–3g) but not in the ERA5 dataset (Figure 3e). In spring, LW_{uw} radiation from ERA-Interim and ERA5 is in good agreement with observations (Figures 5a–5c), as expected from surface temperature agreement between reanalysis and observations. A systematic and strong bias is seen in LW_{net} cooling for ERA-Interim, which originates from a low bias in the downward LW radiation. Thus, the net LW cooling in ERA-Interim can reach -80 Wm^{-2} on daily time scales and can, at times, provide 60 W m^{-2} more cooling than measured during N-ICE2015. This might be due to a low bias in the cloud water content and not to the cloud fraction, which is mostly over 60% in May (Figures 3c–3d) except during the clear sky event on day 143. In contrast, better agreement in both upward and downward components and the net LW radiation is found for the ERA5 and the CERES-SYN datasets (within ±25 W m^{-2}) due to the better reproduction of both surface temperature and cloud properties compared to observations in spring. However, we note a systematic negative bias in LW_{net} for ERA5 in spring, particularly in June, and a positive bias in both LW_{dw} and LW_{net} in ERA5 for day 143 because of an overestimate the COT during the clear sky day, as shown in Figure 4a. The CERES-SYN reproduces well the LW_{net} throughout springtime, but we evidence a compensation between a slight positive bias for LW_{uw} in CERES-SYN before day 140 because of a slight temperature bias and a slight negative bias of LW_{dw}.

Figures 5d–5f shows that the two clear-sky events on days 143 and 166 lead to peaks in the SW radiation in the observations. The duration in particular of the first event seems to be much longer in the ERA-Interim dataset, extending from day 143–152, when the cloud optical thickness remains close to zero (Figure 4a). The temporal resolution of the clear-sky events is better captured by ERA5 and CERES-SYN. Good overall agreement between ERA-Interim, ERA5, and the N-ICE2015 data is observed for both the upward and downward SW radiation before day 145, when we can also assume N-ICE2015 point measurements representative of the ±0.5° grid averages because of the homogeneity of sea ice and albedo over the region, as discussed in Section 3.1.2. For CERES-SYN, the SW_{dw} component is in good agreement with observations before day 145, whereas the SW_{uw} is systematically biased low by up to 50 Wm^{-2} on daily scale.

After day 145, when sea ice melting begins, the N-ICE2015 point data cannot be used anymore as reference, and in fact we observe a significant deviation of both satellite and reanalysis data from surface observations, in particular in the SW_{uw} component. The SW_{uw} is systematically lower (by more than 100 Wm^{-2}) for CERES-SYN between days 145 and 155 compared to reanalysis, while the three data sets agree within their uncertainties afterward, but being always lower than N-ICE2015 point data. The SW_{dw} component is systematically higher for ERA-Interim in the aftermath of the clear sky period between days 144 and 152 compared to ERA5 and CERES-SYN, as anticipated because of the low COT in this dataset. Thereafter the SW_{dw} component is in good agreement between ERA-Interim and ERA5 during June, but higher in CERES-SYN between about days 155–160 because a lower COT, as also identified as negative bias in LW_{dw} data. To note that the sharp peak in ΔSW_{dw} and ΔSW_{uw} seen in all data for day 158 and reaching about 220 Wm^{-2} in CERES-SYN and 140 to 180 Wm^{-2} in ERA5 and ERA-Interim is also the result of only partial N-ICE2015 observations during that day, therefore biasing the observational reference data.

Surface heating due to positive SW_{net} is in good agreement between reanalysis and observations before day 145, while the SW_{net} is larger in CERES-SYN. The CERES-SYN shortwave heating is much larger also compared to reanalysis products after day 145, reflecting the differences in surface albedo as shown earlier. The SW surface net heating can be as large as 120 W m^{-2} on daily time scales for ERA-Interim and ERA5 with peaks of about 180 W m^{-2} as compared to values between 20 and 60 W m^{-2} in the N-ICE2015 observations and an absolute peak of 96 W m^{-2} in the observational dataset. The CERES-SYN surface heating may reach about 200 W m^{-2} on a daily basis.

3.2.3. Winter to Spring Net Radiation Budget

The total net radiation (Figure 5g) shows a steady evolution of the N-ICE2015 net radiation budget over the first 6 months of the year, from a minimum of -60 W m^{-2} in winter to a maximum of 50 W m^{-2} at the end of spring. Results from ERA-Interim and ERA5 for total radiation are in agreement with observations within ±25 Wm^{-2} from the end of winter through the end of May. In June, the differences between ERA datasets and N-ICE2015 reach up to 70 W m^{-2} on daily time scales due to the strong overestimate of the SW$_{net}$ radiation in link with the spatial representativeness of the albedo in N-ICE2015 observations. The CERES-SYN data overestimate the total net radiation in the whole winter to springtime period with differences below 50 W m^{-2} before mid-May and up to 120 W m^{-2} afterward compared to N-ICE2015 point observations and up to 80 W m^{-2} compared to reanalysis data. The only exception is the negative bias of total net radiation during winter cloudy period around days 35–40 and day 47.

3.2.4. Springtime Transition From Sea Ice to Sea Ice Melting Conditions

To have a more detailed view on the variability of the fluxes and the representativeness of average values for evolving surface state and ice conditions, we have reported in Figures 7 and 8 the histograms of SW and LW fluxes derived for three 5-days periods, regularly spaced from end of April to early June, from reanalysis data and N-ICE2015 observations. These periods correspond to days 115–120, 135–140, and 155–160, representative of homogeneous sea ice conditions over the studied region (115–120, 135–140) and the sea ice melting period (155–160). The figures illustrate that while the distribution of LW radiation is basically monomodal around average values for all datasets, the distribution of SW data is more flat because of the stronger variation of SW radiation in link with solar zenith angle, clouds, and surface albedo. Therefore, average values for SW radiation are affected by larger uncertainties than LW data to represent variation in irradiance levels over daily scales. However, this does not affect the identified biases. For instance, during period 115–120 both SW$_{dw}$, SW$_{uw}$, and LW$_{dw}$ are biased low in ERA-Interim, and this is the result of albedo and COT underestimation, as illustrated both as histograms in the investigated regions/time period in Figures S2 and S3 of the supporting information, while the bias is lower in ERA5 data compared to observations. The period 135–140 is affected by a stronger underestimation of COT for liquid clouds by ERA-Interim data compared to ERA5, as evidenced by both histograms (Figure S3) and daily averages (Figure 4), and this induces a strong negative bias in LW radiation and a positive bias in the SW field, while surface albedo differences play a minor role. For the days 155–160, when sea ice melting is taking place over the analyzed area, the reanalysis products show differences from point SW N-ICE2015 data, and a lower bias compared to observations is obtained for LW$_{dw}$ and LW$_{net}$ from reanalysis.

3.2.5. Monthly Means

Table 1 summarizes all the monthly means from N-ICE2015, ERA-Interim, ERA5, and CERES-EBAF/SYN data and their differences for the months of February, May, and June. Analysis of monthly means allows quantification of significant biases at longer time scales. The N-ICE2015 observations are in good agreement with the SHEBA results (Graham et al., 2017a).

To compare the monthly CERES-EBAF (and ERA-Interim/ERA5) and N-ICE2015 observations, we report SW, LW, and net radiation differences (ΔSW, ΔLW, and Δnet, respectively) and their downward and upward components in Figure 6 also for monthly CERES data.

During winter, the CERES-EBAF total net radiation is about 10 W m^{-2} lower (in absolute value) than observations from N-ICE2015. This is due to the upward and downward fluxes exceeding observations because of warmer surface temperatures, and COT that are too large during clear periods, as in the CERES-SYN data. As seen in Figures 6c and 6f, the retrieved CERES-EBAF (and ERA-Interim) net SW and LW fluxes show opposite biases of about 25–30 W m^{-2} with respect to observations in May, in contrast to CERES-SYN that is, biased only in the SW component by 45 W m^{-2} over the monthly mean, and ERA5 that shows opposite but much lower biases (of the order of 10 W m^{-2} or less) in SW and LW net fluxes. The CERES-EBAF LW bias is again possibly due to a warm surface temperature bias, a bias that is not detected in the daily SYN data, which might possibly be the result of flux adjustments in the EBAF retrieval. The SW bias in EBAF data

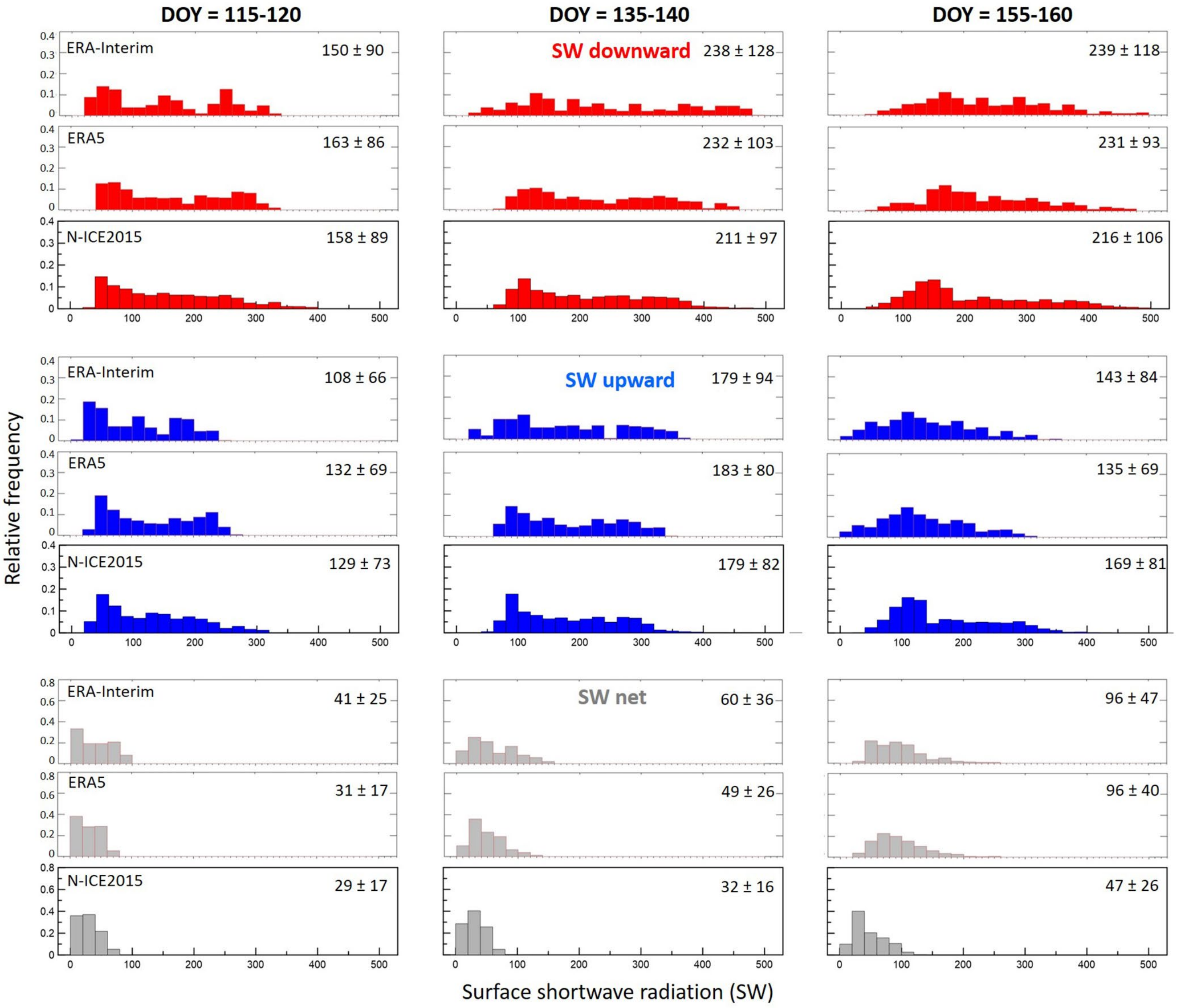

Figure 7. Histograms showing the relative occurrence of the SW downward, upward, and total net radiation measured during N-ICE2015 for the three different 5-days selected periods and retrieved from ERA-Interim and ERA5 data over the ±0.5° region around N-ICE2015 position. The three periods correspond to the day of the year (DOY) intervals 115–120 (25th to 30th April), 135–140 (15th to 20th May), and 155–160 (4th–9th June). Averages and standard deviation of the radiation components over the five days intervals are reported in each plot (units are Wm^{-2}). ERA, ECMWF reanalysis; N-ICE2015, Norwegian young sea ICE 2015.

is due to the underestimation of the surface albedo. However, the albedo from the EBAF data is closer to observations than that for the SYN data, so the net SW bias is lower for EBAF than for SYN. The LW_{net} from CERES-EBAF is comparable to ERA-Interim in May but they are both biased for different reasons: surface temperature is causing the bias in CERES-EBAF, whereas cloud properties are mostly biasing ERA-Interim (as for example in May, during the cloud biased periods as previously discussed). This bias appears to be maintained in June in CERES-EBAF (in contrast to CERES-SYN) in LW_{uw} data, combined with a possible bias in cloud properties although much reduced in the analyses.

Similar biases are observed in the SW budget from the end of April through May (prior to the clear skies on day 143) but are of opposite sign. From the end of May and throughout June, SW_{net} biases increase in ERA-Interim and ERA5 starting around day 145 (25 May) (SW_{net} being between 30 and 80 Wm^{-2} higher than N-ICE2015), which means a significantly larger surface heating linked with sea ice melting in the

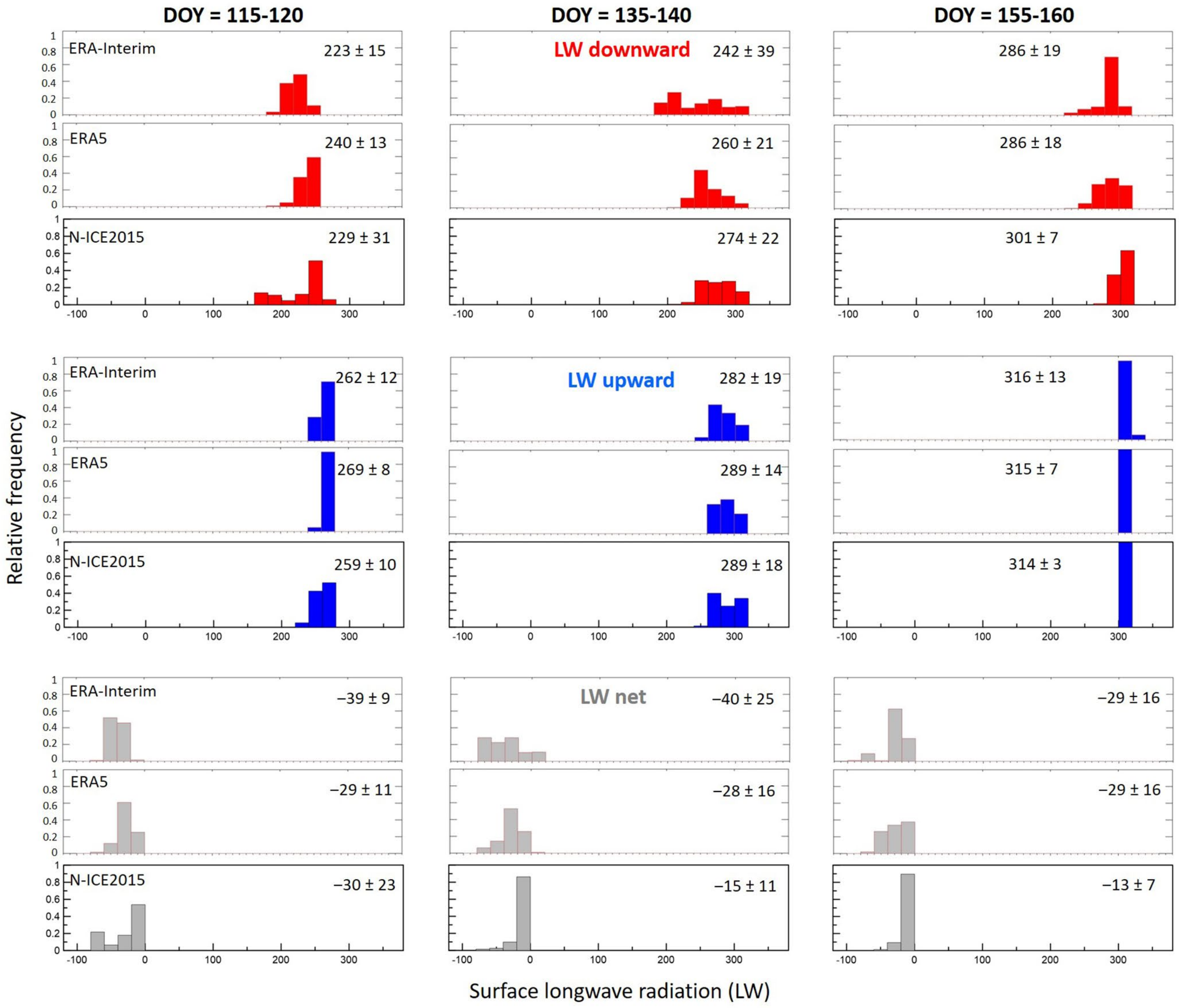

Figure 8. Same as Figure 7 for LW downward, upward, and total net radiation retrieved from ERA-Interim and ERA5 data and measured during N-ICE2015.

region. The bias in CERES-SYN is even larger due to the strong differences in surface albedo leading to a surface SW_{net} that is higher than the observations by 77 Wm^{-2}. As can be seen from Figure 6, a correction in surface albedo would allow CERES-SYN to maintain a bias comparable to early spring. CERES-EBAF is in good agreement with ERA datasets from the end of May and June (days 150 and after), but in both cases, the SW radiation budget is biased as previously discussed. The SW radiation fluxes in ERA-Interim and ERA5 are indeed highly variable, both in magnitude and sign, during May and June. This is due to the combination of both cloud and albedo effects

3.2.6. Summary of Discrepancies in Radiative Fluxes

In summary from Figure 6 and Table 1, CERES-EBAF overestimates LW_{uw} (about 8 Wm^{-2} in winter and 30 Wm^{-2} in spring). This differs from ERA-Interim and ERA5 overestimating the LW_{uw} in winter only (by about +18 Wm^{-2}), and CERES-SYN having +18 Wm^{-2} in February and +11 Wm^{-2} in May. In February, the net radiation is more negative for ERA-Interim (enhanced cooling of -16 Wm^{-2}) because of the temperature biases, whereas the enhanced cooling reduces to -6 Wm^{-2} for ERA5 because of a compensation with a positive bias in LW_{dw}. The positive COT bias in LW_{dw} dominate CERES-SYN and CERES-EBAF with a net

Table 1

Monthly Means of Irradiances From N-ICE2015, ERA-Interim, ERA5, CERES-SYN, and CERES-EBAF and Associated Differences for the Months of February, May, and June When 19, 27, and 13 days of Measurements From N-ICE2015 Were available

Irradiances (Wm^{-2})	SWdw	SWuw	SWnet	LWdw	LWuw	LWnet	TOTnet
February							
N-ICE2015 (19 days)	-	-	-	180.0 ± 56.1	213.1 ± 37.7	−33.1 ± 21.9	−33.1 ± 21.9
ERA-Interim	-	-	-	182.1 ± 51.7	231.6 ± 25.2	−49.5 ± 29.5	−49.5 ± 29.5
ERA-Interim—N-ICE2015	-	-	-	**2.1**	**18.5**	**−16.4**	**−16.4**
ERA5	-	-	-	191.5 ± 45.3	230.9 ± 26.4	−39.4 ± 23.6	−39.4 ± 23.6
ERA5—N-ICE2015	-	-	-	**11.5**	**17.8**	**−6.3**	**−6.3**
CERES-EBAF	-	-	-	198.4 ± 12	220.7 ± 12	−22.3 ± 17	−22.3 ± 27
CERES-EBAF—N-ICE2015	-	-	-	**18.4**	**7.6**	**10.8**	**10.8**
CERES-SYN	-	-	-	206.8 ± 28.4	231.0 ± 26.8	−24.2 ± 8.2	−24.2 ± 8.2
CERES-SYN—N-ICE2015	-	-	-	**26.8**	**17.9**	**8.9**	**8.9**
May							
N-ICE2015 (27 days)	**229.3 ± 53.0**	**188.2 ± 39.8**	**41.1 ± 13.6**	**244.8 ± 30.2**	**270.6 ± 18.8**	**−25.8 ± 18.5**	**15.3 ± 10.9**
ERA-Interim	261.2 ± 46.5	191.6 ± 26.5	69.6 ± 27.0	214.5 ± 25.8	270.5 ± 18.7	−55.9 ± 15.9	13.7 ± 23.2
ERA-Interim—N-ICE2015	**31.9**	**3.4**	**28.5**	**−30.3**	**−0.1**	**−30.1**	**−1.6**
ERA5	231.6 ± 25.6	180.0 ± 14.6	51.6 ± 20.4	244.1 ± 18.2	276.3 ± 16.7	−32.2 ± 8.0	19.3 ± 19.2
ERA5—N-ICE2015	**2.3**	**−8.2**	**10.5**	**−0.7**	**5.7**	**−6.4**	**4.0**
CERES-EBAF	237.9 ± 14	168.4 ± 16	69.5 ± 21	254.5 ± 12	301.9 ± 12	−47.4 ± 17	22.1 ± 27
CERES-EBAF—N-ICE2015	**8.6**	**−19.8**	**28.4**	**9.7**	**31.3**	**−21.6**	**6.9**
CERES-SYN	229.9 ± 41.5	144.3 ± 39.0	85.6 ± 38.5	256.6 ± 28.9	282.1 ± 18.0	−25.5 ± 18.9	60.1 ± 33.8
CERES-SYN—N-ICE2015	**0.6**	**−43.9**	**44.5**	**11.8**	**11.4**	**0.3**	**44.9**
June							
N-ICE2015 (13 days)	**231.2 ± 57.4**	**180.0 ± 41.7**	**51.2 ± 17.4**	**298.4 ± 12.4**	**313.6 ± 2.3**	**−15.2 ± 12.2**	**36.0 ± 10.9**
ERA-Interim	234.9 ± 63.6	136.6 ± 46.7	98.3 ± 34.6	290.0 ± 16.1	317.1 ± 1.7	−27.1 ± 15.0	71.2 ± 29.0
ERA-Interim—N-ICE2015	**3.7**	**−43.4**	**47.1**	**−8.4**	**3.5**	**−11.9**	**35.2**
ERA5	233.1 ± 50.1	127.2 ± 34.9	105.9 ± 32.4	288.0 ± 15.2	315.9 ± 1.9	−27.9 ± 15.1	78.0 ± 23.2
ERA5—N-ICE2015	**1.9**	**−52.8**	**54.7**	**−10.4**	**2.3**	**−12.7**	**42.0**
CERES-EBAF	240.9 ± 14	111.9 ± 16	129 ± 21	288.4 ± 12	344.2 ± 12	−55.8 ± 17	73.2 ± 27
CERES-EBAF—N-ICE2015	**9.7**	**−68.1**	**77.8**	**−10.0**	**30.6**	**−40.6**	**37.2**
CERES-SYN	258.4 ± 51.5	131.0 ± 43.6	127.4 ± 32.2	288.2 ± 17.3	311.8 ± 3.9	−23.6 ± 15.0	103.7 ± 24.4
CERES-SYN—N-ICE2015	**27.2**	**−49.0**	**76.2**	**−10.2**	**−1.8**	**−8.4**	**67.7**

Note. The number of days of N-ICE2015 data is indicated. The ERA-Interim, ERA5, and CERES-SYN averages are calculated considering only N-ICE2015 measurement days, while CERES-EBAF data are full monthly averages. Monthly means are calculated from daily averages for N-ICE2015, ERA-Interim, ERA5, and CERES-SYN datasets and the reported uncertainties are the 1 standard deviation. Data are in Wm^{-2}. Bold values represent N-ICE2015 observational data and differences for the different datasets.

Abbreviation: CERES, Clouds and the Earth's Radiant Energy System; ERA, ECMWF reanalysis; LW, longwave; N-ICE2015, Norwegian young sea ICE 2015; SW, shortwave.

winter warming in the order of 10 Wm^{-2}. In May and June, CERES-EBAF and CERES-SYN both provide accurate estimates of downward fluxes: SW_{dw} and LW_{dw} differ by less than 12 Wm^{-2} from N-ICE2015 (but increasing to 27 Wm^{-2} for SW_{dw} in June), demonstrating good ability to account for contributions from clouds. However, they still largely underestimate SW_{uw} (in the range 20–40 Wm^{-2} in May). This is in opposition to ERA-Interim which fails to reproduce all components except upward fluxes (LW_{uw} and SW_{uw}) in May, and all components except SW_{dw} and LW_{uw} in June. The net effect is an overestimation of SW_{net} heating and LW_{net} cooling for both CERES and ERA-Interim datasets in May and also in June, even if in June the effect of spatial sampling and sea ice melting prevent a direct comparison with surface point observations particularly for SW radiation. However, the ERA5 monthly means reproduce all components of the radiation budget in May quite well, with differences less than 11 W m^{-2} from N-ICE2015. The LW_{dw} component is biased low in June by 10 W m^{-2} because of an underestimation of the COT for an episode at the beginning of the month between days 155 and 160.

The observed agreement in the total net radiation in May for CERES-EBAF and ERA-Interim is therefore, and differently from ERA5, only due to compensation of errors in the net SW and LW components. In June, on the other hand, both ERA and CERES products overestimate the net total heating by 35–68 Wm^{-2} on a monthly basis mostly due to the failure to reproduce the net SW caused by the differences in surface albedo sampling over the investigated area compared to N-ICE2015 point data.

Therefore, the surface parameters are critical in the comparison of SW fluxes for this location of the field camp when it is close to the marginal ice zone.

4. Discussion

4.1. Surface Fluxes Drivers

As we have shown above, biases in components of the radiation budget might cancel out so that the net radiation is properly represented, but for the wrong reasons. In our case, this is especially obvious in May. The analysis of radiation flux differences conducted above confirms that the different parameters (clouds, albedo, surface temperature) play significant roles in the SW and LW components of the radiation budget and may act differently in the different seasons. Although clouds are key factors for both SW and LW radiation, their roles are different for each component of the radiation budget.

This is confirmed by the fact that only a few significant correlations are obtained between the CERES-SYN dataset and N-ICE2015 (or CALIOP) data set, which is considered as the reference. This is shown by examining the differences of low cloud cover (ΔLCC) or total cloud cover (ΔTCC) separately as shown in Figure 9. Similar results are obtained for ERA-Interim and ERA5 (not shown). Not surprisingly, the quantities that appear to be better correlated are ΔLW_{up} and ΔT ($R^2 = 0.96$ for CERES-SYN, 0.77 for ERA-Interim, and 0.90 for ERA5). The correlation coefficient R^2 is lower than 0.5 in all other cases. The ΔLW_{dw} (Figures 9c and 9d) shows an increase with increasing ΔLCC and ΔTCC. The correlation is, however, poor ($R^2 < 0.30$). In both cases and also for ΔSW_{dw} (Figures 9g and 9h), one can see a large dispersion of the data. This is most probably due to the fact that, together with cloud cover, the liquid and ice water paths that control the radiative effect on LW_{dw} and SW_{dw} radiation are poorly represented. In May, as seen from IAOOS observations, this is expected to be due to the representation of low-level liquid water clouds in ERA-Interim data. The ΔSW_{dw} and ΔSW_{up} terms are insensitive to changes in surface temperature and show a poor correlation with the other parameters. SW_{net} depends on the surface albedo and is modulated by the cloud properties, which, in turn, affect the irradiance SW_{dw} reaching the surface. There may not be a simple relationship because SW_{dw} is also modulated by multiple reflections between the surface and the atmosphere (Di Biagio et al., 2012; Minnis et al., 1993), especially for high surface albedo conditions and during cloudy periods.

One interesting feature is that the total net radiation Δnet sensitivity is absent in surface temperature (Figure 9i) but not in the albedo (Figure 9j). This is also the case for the low-level (LCC) and the total cloud fraction (TCC), although some dependence is seen on the net longwave radiation ΔLW_{net}. This is, in fact, not surprising given the results given in Figure 5 that albedo plays a similar role for SW_{up} and SW_{dw} in cloudy conditions, whereas most of the radiative impact of clouds is of opposite sign for LW_{net} and SW_{net}.

Relating the components of the differences in the SW and LW radiation field from reanalysis and observations for the April-June period, we look for systematic biases in surface properties taking advantage of random variability in cloud contributions in the various datasets. Results are reported in Figure 10 for (a), (d), (g) ΔLW_{dw} and ΔLW_{uw}, (b), (e), (h) ΔSW_{dw} and ΔLW_{dw}, (c), (f), (i) for ΔSW_{dw} and ΔSW_{uw}. The biases and variability in panels (a), (d), and (g) depend on surface temperature and cloud properties. As reported in Table 1 (and discussed in Section 3.2), we do not expect ΔLW_{uw} to be biased in early spring (the difference is a few Wm^{-2}, which is considered to be within the error in our analysis). The bias is rather observed in ΔLW_{dw} as shown in Figure 5, with an average value of about -13.9 Wm^{-2} for ERA-Interim, and −1.7 $W.m^{-2}$

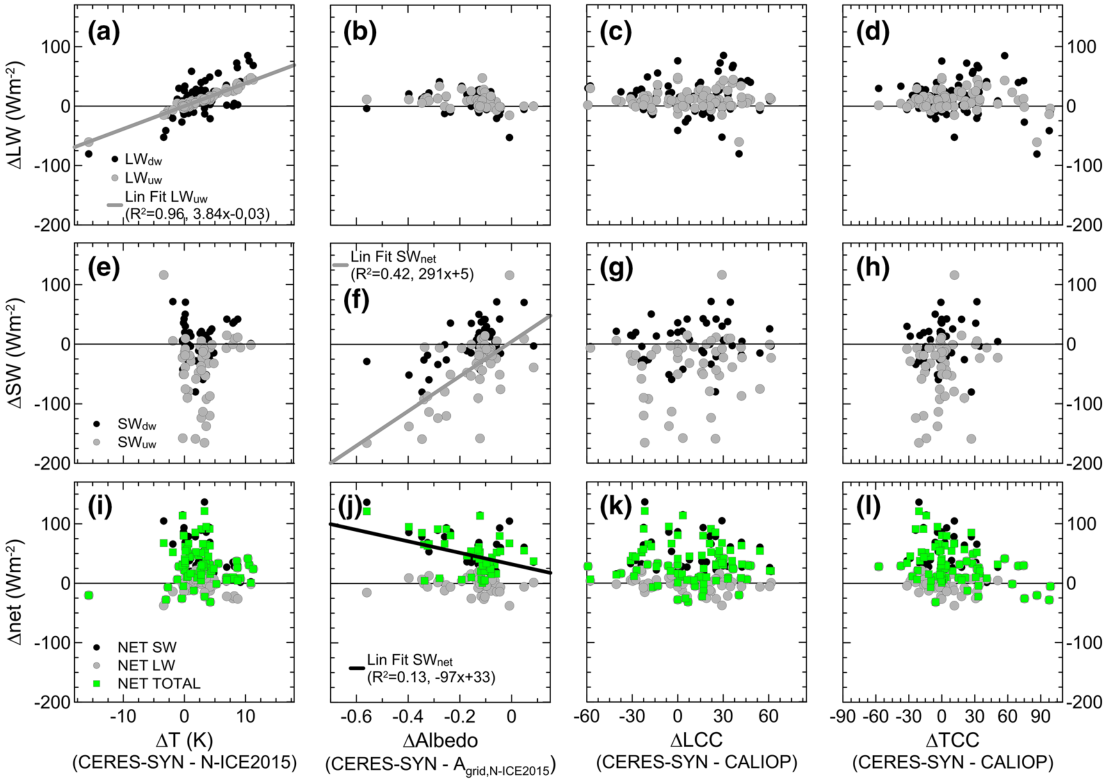

Figure 9. Differences between CERES-SYN and N-ICE2015 radiation data in winter and spring (first row ΔLW_{dw} and ΔLW_{uw}, second row ΔSW_{uw} and ΔSW_{dw}, third row SW_{net}, LW_{net} and net total) versus difference in surface temperature between CERES-SYN and N-ICE2015 (first column ΔT), the surface albedo from CERES-SYN and gridded N-ICE2015 albedo (second column ΔAlbedo), and the difference in low and total cloud cover between CERES-SYN and CALIOP (third and fourth columns ΔLCC, ΔTCC, respectively). Data are reported as daily averages for the whole dataset. The outlier point $\Delta SW_{dw} = 220$ Wm^{-2} identified in the CERES-SYN dataset in Figures 5 and 6 for day 158 is eliminated from the dataset. The number of data points is between 49 and 80 for the different plots. CALIOP, Cloud and Aerosol Lidar with Orthogonal Polarization; CERES, Clouds and the Earth's Radiant Energy System; LW, longwave; N-ICE2015, Norwegian young sea ICE 2015; SW, shortwave.

for ERA5, as shown in Figures 10b and 10e, corresponding to the average LW_{dw} bias between May and mid-June. The linear dependence found in the plot between ΔLW_{uw} and ΔLW_{dw} is due to the common source of variability on cloud distribution linking the two datasets. However, the correlation is not good for CERES-SYN (0.31), and only slightly better for ERA-Interim (0.50), and ERA5 (0.61). Taking into account the bias in ΔLW_{dw} in the (ERA-Interim (and ERA5) minus N-ICE2015) distribution leads to get a more symmetric distribution. One should note that it is the reverse in the (CERES-SYN - N-ICE2015) distribution. Now let us consider central panels of Figures (10b, 10e, and 10h**)**, reporting the variation of the longwave ΔLW_{dw} as a function of shortwave downward difference ΔSW_{dw}. In this case, the driver of variability is only the cloud properties (and the optical depth at first order). A better correlation ($R^2 = 0.82$) is obtained for ERA-Interim, while the correlation is lower in ERA5 (0.68) and poor (0.29) for CERES-SYN confirming that clouds are not the main driver of variability during spring for CERES, as expected from the good representation of the COT compared to observations (see Figure 4). In Figures 10a and 10d as well as in Figures 10b and 10e, one can see that results for ERA-Interim and ERA5 are comparable. The dispersion of points appears slightly better for ERA-Interim. The slope giving the sensitivity with cloud properties for ERA-Interim and ERA5 shows that SW sensitivity is about twice that for LW (Figures 10b and 10e). The ΔLW_{dw} varies from about +40 to -70 Wm^{-2}. However, a larger bias in ΔLW_{dw} is seen in ERA-Interim that implies correcting the offset in ΔLW_{dw} by about -13.9 Wm^{-2}, to obtain to a distribution better centered around zero. For ERA5, the correction is reduced to about -1.7 Wm^{-2}. The bias in ΔSW_{dw} is closer to zero (but ~ 10 Wm^{-2}) in line with average biases for May and June in Table 1. Given that the effect on SW radiation is mostly due to the COT and is well centered, then the total average COT is expected to be unbiased for both ERA reanalysis. Note that from Figure 4, higher June values compensate lower May values in ERA-Interim. On the other side, the dispersion of points in Figure 10h for CERES-SYN is more centered and extreme values may be

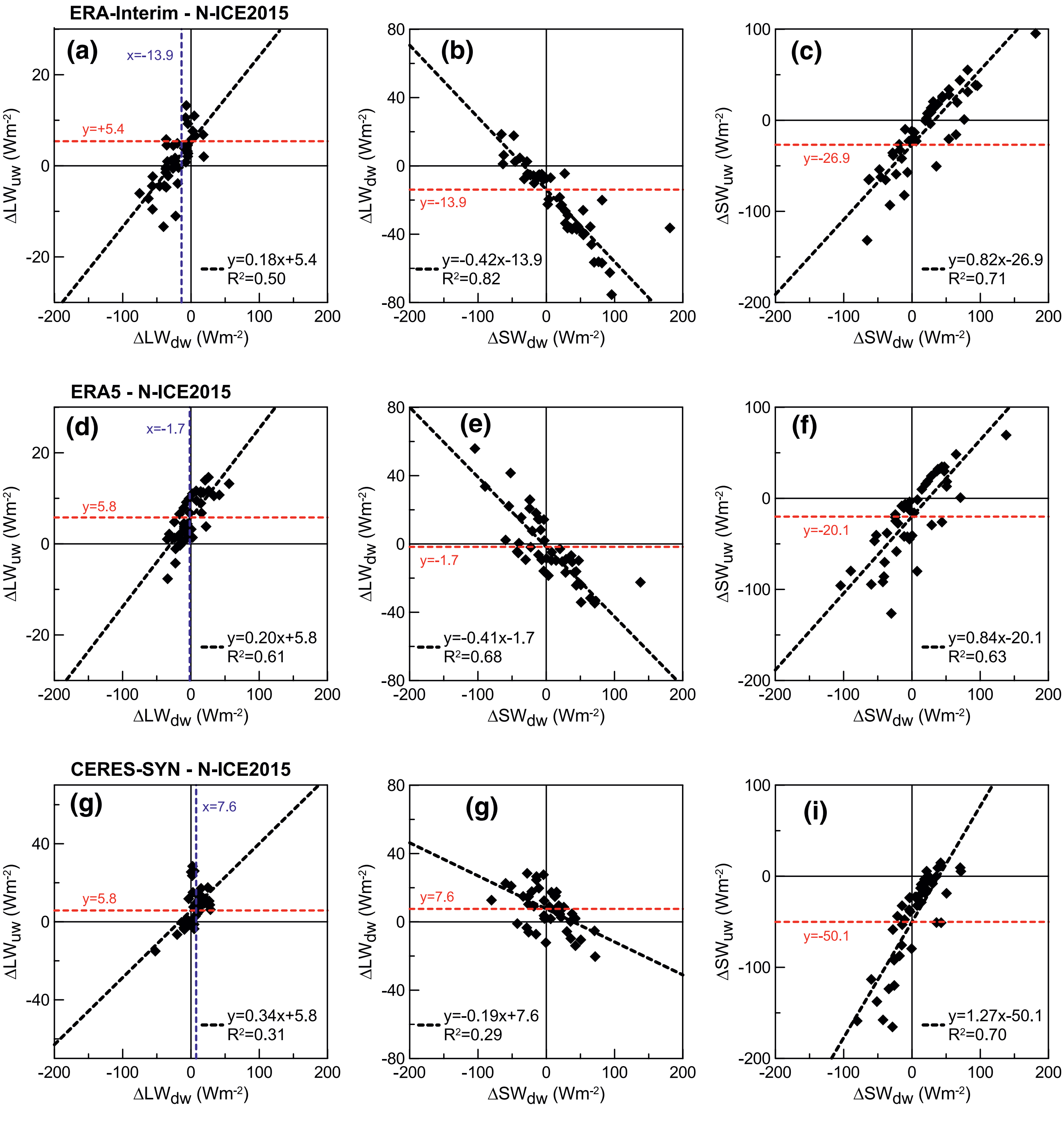

Figure 10. (a, d, and g) Upward longwave irradiance differences between ERA-Interim/ERA5/CERES-SYN and N-ICE2015 (ΔLW_{uw}) versus downward longwave irradiance differences (ΔLW_{dw}) estimated from spring to summer time (25 April–18 June). (b, e, and h) Downward longwave irradiance differences (ΔLW_{dw}) versus the downward shortwave irradiance differences (ΔSW_{dw}). (c, f, and i) Upward shortwave irradiance differences (ΔSW_{uw}) versus the ΔSW_{dw}. Data are reported as daily averages. The linear fits between the dataset and the correlation coefficients of the fits are indicated. Dashed horizontal red lines correspond to average bias in surface temperature and altitude of low clouds in ERA-Interim, ERA5 and CERES-SYN data. Dashed vertical blue lines in panels (a, d, and g) indicate LW_{dw} bias retrieved in panels (b, e, and h). Error bars are not shown for the sake of clarity. The outlier point ΔSW_{dw} = 220 Wm^{-2} identified in the CERES-SYN dataset in Figures 5 and 6 for day 158 is eliminated from the dataset. CERES, Clouds and the Earth's Radiant Energy System; ERA, ECMWF reanalysis; LW, longwave; N-ICE2015, Norwegian young sea ICE 2015; SW, shortwave.

more representative of temperature differences (related to the surface and cloud altitude). This is only true to the first order, as cloud microphysics play an additional role. There may be, however, second-order compensations between the optical depth and the cloud microphysics (cloud water and ice partition), and differences in the aerosol contribution. Figures 10c, 10f, and 10i show that the residual bias would then be in ΔSW_{uw} as expected from the biased albedo. It leads to an average value close to -27 W m^{-2} for ERA-Interim, -20 W m^{-2} for ERA5 and -50 W m-^{2} for CERES-SYN.

A more detailed analysis would be required on a more extended dataset to explore this further, but what comes out from this analysis is that besides surface albedo and temperature, observed differences in fluxes are mostly associated to the combination of cloud layer properties, e.g. their altitude and individual optical depth in a more critical way in ERA-Interim reanalysis and CERES, in particular in June.

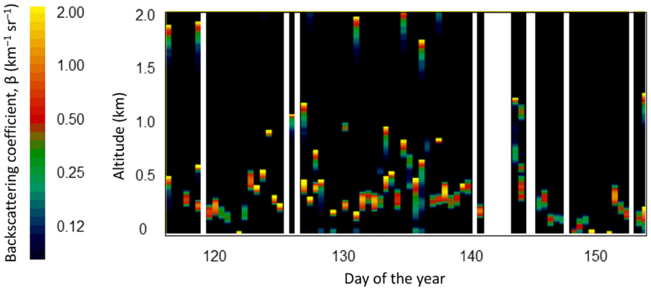

Figure 11. 2D plot of the retrieved backscattering coefficient measured from end of April to beginning of June 2015 by the IAOOS lidar. White stripes are for no or no valid data. As shown by the color code, rapid variation and high backscattering is representative of water clouds, whereas smoother variations (days 135–136) and lower values are more representative of ice (possibly precipitating from super-cooled clouds). IAOOS, Ice-Atmosphere-Arctic Ocean Observing System.

4.2. Clouds

As seen in Figure 4, the downward irradiance calculated by ERA-Interim and ERA5 results from the combination of low-level water clouds and elevated ice clouds. The total water and ice cloud contents are small in May, varying from 0.001 to 0.01 kg m^{-2} for both water and ice in reanalysis. They are close to 0.01 kg m^{-2} more than 50% of the time (between days 125 and 135 for ERA5, and days 143 and 151 for both products). Larger values are determined in June. Using relationships between microphysical and optical cloud properties (see Section 2.3), water and ice cloud COTs were derived (and reported in Figure 4) assuming that the effective radius of the cloud droplets is equal to 10 μm for liquid droplets and 30 μm for ice particles. The COT values derived for May are close to 0.7, except for days 136–142 where they are about 2 on average for ERA-Interim. In June, when temperatures are warmer and close to zero (Cohen et al., 2017), COTs are about 2 and 8 for water and ice clouds, respectively (see Figure 4). Larger values of COT for liquid and ice clouds are obtained for ERA5 in agreement with CERES and RTC calculations based on radiation and meteorological measurements. To note that while we used a fixed R_{eff} for estimate of the COT from reanalysis, the CERES algorithm adjust the R_{eff} value based on MODIS observations in its retrieval.

Ten minutes daily IAOOS lidar observations (up to 4 per day at 3, 9 am and pm, but more frequently twice a day as limited by data transmission) reported in Figure 3 show a large occurrence of low clouds. Their apparent vertical extent, as reported in Figure 11 below 1.5 km in altitude, is mostly varying from about 200 m to 1,000 m above the surface. This upper altitude corresponds to the vertical extent of the boundary layer, as reported in Figure S5 showing vertical profiles of temperature, potential temperature and relative humidity (RH) derived from radiosonde measurements and ERA5 re-analysis for May 15th (day 135). The measured RH is peaking at more than 90% at 1 km, and is slightly larger than ERA5. Figure 11 shows that cloud base as detected by lidar is mostly near 0.3 km, where the temperature is close to 266 K (temperature at 500 m from both from radiosonde and ERA5). The color code is indicative of the maximum backscattering coefficients β_{max} observed (between 0.5 and 2 $km^{-1}sr^{-1}$). The reduced vertical extent is caused by large extinction in optically-dense clouds as the laser beam propagation is rapidly attenuated by scattering through the cloud, and this effect cannot be corrected in the upper part of the cloud by the inversion algorithm. These strongly peaked backscattering coefficients are observed over a thickness of about $\Delta z = 100$ m (at half maximum). They are the signature of liquid water clouds, where droplets much smaller in size than ice crystals induce larger bakscattering and extinction (Pinnick et al., 1983; Spinhirne et al., 1989). The related extinction coefficients can be derived using a ratio S_c equal to = 18.2 sr fairly constant with size for liquid water droplets (Pinnick et al., 1983). The estimated COT (retrieved here from the apparent cloud thickness as equal to $S_c\, \beta_{max}\, 2\Delta z \sim 4\, \beta_{max}$), in such conditions is expected to be of the order of six and larger for the points with β_{max} equal to or larger than 1.5 $km^{-1}sr^{-1}$ (orange and yellow color codes, respectively), down to about 2 for the 0.5 $km^{-1}sr^{-1}$ values (red color code). These optical depths are minimum estimates for these boundary layer clouds, as the apparent cloud thickness is limited by penetration into the cloud. They are however much larger than those given by ERA-Interim reanalysis (very frequently smaller than 1) in the

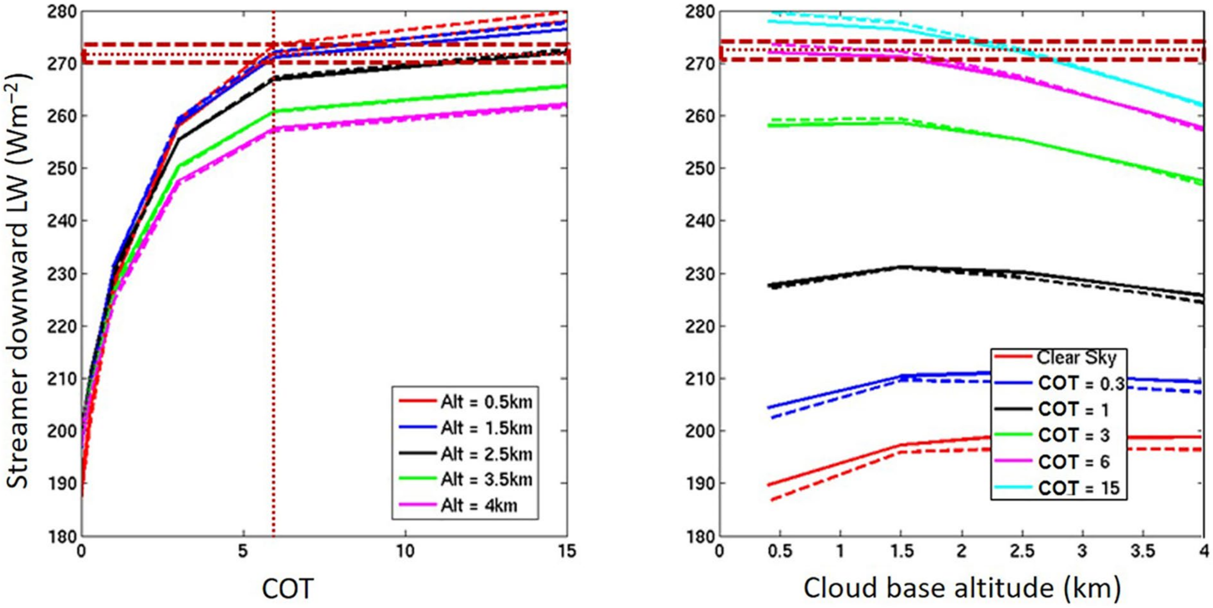

Figure 12. LW downward radiation fluxes calculated with the RTC Streamer assuming a water cloud layer of 500 m thickness of variable altitude and optical thickness. The horizontal dotted line indicates the surface measurements of LW downward irradiance with its uncertainty of 2 Wm^{-2} (indicated with dashed lines). COT, cloud optical thickness; LW, longwave; RTC, radiative transfer code.

considered period of May (days 135–140), but are more in agreement with all other COTs corresponding to water clouds (see Figure 4) including ERA5 reanalysis.

Clouds with COTs smaller than about 10 are not opaque to LW radiation. The emitted LW radiation of such a gray body at a temperature Tc is $LW = \varepsilon\sigma Tc^4$. The measured LW_{dw} radiative flux of 271 Wm^{-2} thus corresponds to an average emissivity $\varepsilon \sim 0.95$ for a T_c of 266 K. Cloud emissivity ε and CLW are in fact linked to the IR COT (τ_{IR}) by the relationship $\varepsilon = 1\text{-}\exp(-\tau_{IR})$ and ($-\tau_{IR} \sim 158$. CLW) according to Mie theory, assuming only absorption in the thermal infrared is half the COT in the visible domain (Stephens, 1978). A value in emissivity of 0.95, as estimated before, thus corresponds to a COT of about 6 in agreement with radiation and lidar estimates. This is confirmed by the sensitivity analysis performed with the radiative transfer code Streamer. Figure 12 shows LW_{dw} fluxes at the surface determined with Streamer for various liquid water cloud properties (single cloud layer which altitude is ranging from 0.5 to 4 km, and COT varying from 0.3 to 15) in a single cloud layer 500 m thick. Temperature and moisture profiles are taken from ERA5 (Figure S5). This sensitivity analysis shows that surface measurements (reported as dashed line and an uncertainty of 2 Wm^{-2}) are corresponding to low level clouds with COTs larger than 6. An upper altitude layer (at an altitude of 2.5 km) with larger COT is possible, but as located in low RH region, it can be excluded.

As a result from the convergence between observations and reanalysis, one can concur that the bias in ERA-Interim LW_{dw} irradiance is caused by the fact that the CLW of the low-level super-cooled clouds is too small in the analysis. This bias in CLW is much reduced in ERA5. The CERES observations appear to be overestimating LW_{dw} fluxes which may be attributed in springtime to larger COTs and higher altitude attribution as identified by Blanchard et al. (2014).

Considering the period of June, it appears (see Table 1) that LW_{dw} is this time biased low with respect to observations for all ERA analyses and CERES products. Clouds remains therefore an issue for all datasets.

5. Conclusions

State-of-the-art gridded reanalysis datasets (ERA-Interim/ERA5) and remote sensing observations (CERES-EBAF/SYN) have been compared to local-scale remote sensing observations of radiation fields, using surface albedo, cloud distribution, and meteorology from N-ICE2015, IAOOS, and CALIOP between January and June 2015. Observations during N-ICE2015 were taken in the synoptically active North Atlantic sector of the Arctic Ocean, north of Svalbard, in rather thin and young sea ice conditions (Granskog et al., 2018).

The conditions encountered during the N-ICE2015 field campaign, that is, the alternation of "cloudy opaquely" and "radiatively clear" states in wintertime (Graham et al., 2017a) and persistent low clouds in springtime, are nonetheless well representative of the Arctic basin.

Our results confirm previous findings (e.g., Graham et al., 2019; Liu & Key, 2016) which showed that atmospheric reanalysis, in particular ERA-Interim, exhibit significant differences in their simulation of Arctic clouds and radiation compared to local scale observations. Better performance of ERA5 is found because of the improvement of cloud representation. In particular, biases in liquid water content in boundary-layer super-cooled and water clouds in ERA-Interim are suppressed in ERA5. We also highlight differences in satellite observations from CERES-SYN/EBAF compared to local scale datasets despite their better representation of cloud distribution, but mostly related in our study to surface albedo parameters, and possible biases in surface temperature. In the past, CERES data have been used as reference observations for Arctic radiation and energy budget studies (see Boeke & Taylor, 2016; Hegyi & Taylor, 2017). Nonetheless our results indicate that early spring albedo values are slightly biased low. Caution is also required in fragmented sea-ice, when using these data in particular in regions close to the sea-ice edge. In this sense, and given the growing extent of Arctic ice covers seasonal melting, it is expected that this issue could be of relevance for an increasing portion of the Arctic Ocean covered with ice.

We stress here that the analysis of the differences over sea ice has to be performed with prudence, since part of the differences can be explained between the point observations made on snow-covered sea ice during N-ICE2015 and average values over grid cells that are output by the satellite retrievals and/or re-analyses. The latter include a small but important open water fraction, especially for more fragile younger sea-ice (Graham et al., 2019). As a matter of fact, our analysis shows the need of observational data separating the contribution of ice and open waters to surface albedo in grid cells, with possibly several flux measurements points. We show here that the calculated gridded albedo accounts for this heterogeneity, but still remains higher than the one from reanalysis and satellite observations. High resolution surface data are available from synthetic aperture radar but are not included in standard analyses. This would be crucial for better comparing to field observations and understanding processes driving the surface radiation budget, but also they would be particularly useful to improve atmospheric models with more precise sea-ice distribution. This is of particular importance in the present changing Arctic sea-ice conditions.

Our observations further highlight the necessity to improve cloud parametrizations in models, which allow a larger liquid water content in boundary-layer clouds in the Arctic system. Previous studies have already been conducted at ECMWF that change cloud phase parametrization to enable more water to be produced in super-cooled low-level clouds (Forbes et al., 2016). This model improvement reduces SW biases in frontal clouds at high latitudes. Assimilation of better albedo and surface temperature from microwave, infrared and visible satellite radiometry should allow reduction of residual biases. To achieve these goals, satellite observations are required, but, as shown in this study, they need to offer high vertical resolution, and local-scale data over the high Arctic Ocean remain of vital importance. This is particularly true for boundary-layer clouds due to the fact that CALIPSO and CloudSat data are limited to 82°N. With atmospheric observations started in 2014 and operated for over 5 years, IAOOS database is aiming at providing more statistical information on surface properties and aerosols/cloud occurrence and phase over the high Arctic Ocean where there are limited observations. New capabilities on downward radiation measurements (sky brightness temperature and downward SW radiation) have been added to IAOOS platforms after N-ICE2015 that should able to improve data analyses in more recent deployments. These data and observations from new experiments such as the MOSAIC expedition (https://www.mosaic-expedition.org) will provide unique constraints for regional and global models and for improving satellite and reanalysis datasets in this region, which is sensitive to climate change.

Data Availability Statement

The N-ICE2015 observational data sets are available from the Norwegian Polar Data Center (https://data.npolar.no/dataset/) and are cited in the text (Hudson et al., 2015, 2016, 2017). The IAOOS atmospheric data used in this paper are available upon request to the corresponding author and are available through the AERIS

Data Portal at https://www.aerisdata.fr/. The CALIPSO and CERES data used in this study are available from NASA at https://eosweb.larc.nasa.gov/. The CALIPSO data are also available in France in the AERIS/ICARE Data Portal at http://www.icare.univ-lille1.fr/. The ERA-Interim reanalysis and the ECMWF operational analysis products can be retrieved at from http://apps.ecmwf.int/. The ERA5 data can be downloaded the Copernicus Climate Change Service (C3S) Climate Date Store (https://cds.climate.copernicus.eu/#!/search?text=ERA5&type=dataset). Documentation of the ERA-Interim products can be found at (https://www.ecmwf.int/en/forecasts/datasets/reanalysis-datasets/era-interim) and at https://cds.climate.copernicus.eu/cdsapp#!/dataset/reanalysis-era5-single-levels?tab=overview andhttps://confluence.ecmwf.int/display/CKB/ERA5 for the ERA5 used products. The CERES-SYN and CERES-EBAF products are available from NASA/LaRC at https://ceres.larc.nasa.gov/compare_products.php. Sea ice concentration data from AMSR2 observations can be found at https://seaice.uni-bremen.de/sea-ice-concentration-amsr-eamsr2/.

Acknowledgments

This work was partly supported by funding from the ICE-ARC program from the European Union 7th Framework Programme, grant 603887, ICE-ARC contribution number 072, when the first author was on postdoctoral grant at LATMOS. The IAOOS program has been funded by the Agence Nationale de la Recherche (ANR-10-EQPX-32-01) and has been developed in partnership with LOCEAN at SU/UPMC. We thank the DT/INSU/CNRS for the deployment, and survey of the IAOOS platforms during the first two periods of N-ICE2015. We would like to particularly thank DT/INSU Brest for their involvement during these two periods, and the help of our LOCEAN and NPI colleagues for the last period. The N-ICE2015 field experiment was supported by the Norwegian Polar Institute's Centre for Ice, Climate and Ecosystems (ICE) through the N-ICE project. V. P. Walden acknowledges support from the U.S.-Norway Fulbright Arctic Chair program and Washington State University. Radiative modeling benefited from access to IDRIS HPC resources (GENCI allocations A003017141 and A005017141) and the IPSL mesoscale computing center (CICLAD: Calcul Intensif pour le CLimat, l'Atmosphère et la Dynamique). NASA, CNES, the ICARE/AERIS and the LARC data centers are gratefully acknowledged for supplying the CALIPSO and CERES data. The authors wish to acknowledge the three anonymous reviewers for their comments that helped to improve the manuscript.

References

Bintanja, R., & Krikken, F. (2016). Magnitude and pattern of Arctic warming governed by the seasonality of radiative forcing. *Scientific Reports*, *6*, 38287. https://doi.org/10.1038/srep38287

Blanchard, Y., Pelon, J., Eloranta, E. W., Moran, K. P., Delanoë, J., & Sèze, G. (2014). A synergistic analysis of cloud cover and vertical distribution from A-Train and ground-based sensors over the high Arctic station Eureka from 2006 to 2010. *Journal of Applied Meteorology and Climate*, *53*, 2553–2570. https://doi.org/10.1175/JAMC-D-14-0021.1

Boeke, R. C., & Taylor, P. C. (2016). Evaluation of the Arctic surface radiation budget in CMIP5 models. *Journal of Geophysical Research: Atmospheres*, *121*, 8525–8548. https://doi.org/10.1002/2016JD025099

Bourassa, M. A., Gille, S. T., Bitz, C., Carlson, D., Cerovecki, I., Clayson, C. A., et al. (2013). High-Latitude ocean and sea ice surface fluxes challenges for climate research. *Bulletin of the American Meteorological Society*, *94*, 403–423. https://doi.org/10.1175/BAMS-D-11-00244.1

Cesana, G., Kay, J. E., Chepfer, H., English, J. M., & de Boer, G. (2012). Ubiquitous low-level liquid-containing Arctic clouds: New observations and climate model constraints from CALIPSO-GOCCP. *Geophysical Research Letters*, *39*, L20804. https://doi.org/10.1029/2012GL053385

Chen, H., Schmidt, S., King, M. D., Wind, G., Bucholtz, A., Reid, E. A., et al. (2019). Shortwave radiative effect of arctic low-level clouds: Evaluation of imagery-derived irradiance with Aircraft observations. *Atmospheric Measurement Techniques Discussions* in review. https://doi.org/10.5194/amt-2019-344

Cohen, L., Hudson, S. R., Walden, V. P., Graham, R. M., & Granskog, M. A. (2017). Meteorological conditions in a thinner Arctic sea ice regime from winter to summer during the Norwegian Young Sea Ice expedition (N-ICE2015). *Journal of Geophysical Research: Atmospheres*, *122*, 7235–7259. https://doi.org/10.1002/2016JD026034

Dee, D. P., Uppala, S. M., Simmons, A. J., Berrisford, P., Poli, P., Kobayashi, S., et al. (2011). The ERA-Interim re-analysis: Configuration and performance of the data assimilation system. *Quarterly Journal of the Royal Meteorological Society*, *137*, 553–597. https://doi.org/10.1002/qj.828

Di Biagio, C., di Sarra, A., Eriksen, P., Ascanius, S. E., Muscari, G., & Holben, B. (2012). Effect of surface albedo, water vapor, and atmospheric aerosols on the cloud-free shortwave radiative balance in the Arctic. *Climate Dynamics*, *39*(3), 953–969. https://doi.org/10.1007/s00382-011-1280-1

Di Biagio, C., Pelon, J., Ancellet, G., Bazureau, A., & Mariage, V. (2018). Sources, load, vertical distribution, and fate of wintertime aerosols north of Svalbard from combined V4 CALIOP data, ground-based IAOOS lidar observations and trajectory analysis. *Journal of Geophysical Research: Atmosphere*, *123*, 1363–1383. https://doi.org/10.1002/2017JD027530

Doelling, D. R., Loeb, N. G., Keyes, D. F., Nordeen, M. L., Morstad, D., Nguyen, C., et al. (2013). Geostationary enhanced temporal inpterpolation for CERES flux products. *Journal of Atmospheric and Oceanic Technology*, *30*, 1072–1090. https://doi.org/10.1175/JTECH-D-12-00136.1

Döscher, R., Vihma, T., & Maksimovich, E. (2014). Recent advances in understanding the Arctic climate system state and change from a sea ice perspective: A review. *Atmospheric Chemistry and Physics*, *14*, 13571–13600. https://doi.org/10.5194/acp-14-13571-2014

Feldman, D. R., Collins, W. D., Pincus, R., Huang, X., & Chen, X. (2014). Far-infrared surface emissivity and climate. *Proceedings of the National Academy of Sciences*, *111*(46), 16297–16302. https://doi.org/10.1073/pnas.1413640111

Forbes, R., Geer, A., Lonitz, K., & Ahlgrimm, M. (2016). *Reducing systematic errors in cold-air outbreaks*. In ECMWF Newsletter. (Vol. 146, pp. 17–22). Reading, UK: ECMWF https://doi.org/10.21957/s41h7q7l

Graham, R. M., Cohen, L., Petty, A. A., Boisvert, L. N., Rinke, A., Hudson, S. R., et al. (2017b). Increasing frequency and duration of Arctic winter warming events. *Geophysical Research Letters*, *44*, 6974–6983. https://doi.org/10.1002/2017GL073395

Graham, R. M., Cohen, L., Ritzhaupt, N., Segger, B., Graversen, R. G., Rinke, A., et al. (2019). Evaluation of six atmospheric reanalyses over Arctic sea ice from winter to early summer. *Journal of Climate*, *32*(14), 4121–4143. https://doi.org/10.1175/JCLI-D-18-0643.1

Graham, R. M., Rinke, A., Cohen, L., Hudson, S. R., Walden, V. P., Granskog, M. A., et al. (2017a). A comparison of the two Arctic atmospheric winter states observed during N-ICE2015 and SHEBA. *Journal of Geophysical Research: Atmospheres*, *122*, 5716–5737. https://doi.org/10.1002/2016JD025475

Granskog, M. A., Fer, I., Rinke, A., & Steen, H. (2018). Atmosphere-ice ocean-ecosystem processes in a thinner Arctic sea ice regime: The Norwegian young sea iCE (N-ICE2015) expedition. *Journal of Geophysical Research: Oceans*, *123*, 1586–1594. https://doi.org/10.1002/2017JC013328

Han, Q., Rossow, W. B., & Lacis, A. A. (1994). Near-Global survey of effective droplet radii in liquid water clouds using ISCCP data. *Journal of Climate*, *7*, 465–497.

Hegyi, B. M., & Taylor, P. C. (2017). The regional influence of the Arctic Oscillation and Arctic Dipole on the wintertime Arctic surface radiation budget and sea ice growth. *Geophysical Research Letters*, *44*, 4341–4350. https://doi.org/10.1002/2017GL073281

Hersbach, H., Bell, B., Berrisford, P, Hirahara, S., Horányi, A., Muñoz-Sabater, J., et al. (2020). The ERA5 global reanalysis. *Quarterly Journal of the Royal Meteorological Society*, *146*(730), 1999–2049.

Hersbach, H., Bell, B., Berrisford, P., Horányi, A., Muñoz Sabater, J., Nicolas, J., et al. (2019). *Global reanalysis: Goodbye ERA-Interim, hello ERA5, ECMWF Newsletter*. (Vol. 159, pp. 17–24). Reading, UK: ECMWF.

Hudson, S. R., Cohen, L., Kayser, M., Maturilli, M., Kim, J., Park, S., et al. (2017). *N-ICE2015 atmospheric profiles from radiosondes [Data set]*. Norwegian Polar Institute. https://doi.org/10.21334/npolar.2017.216df9b3

Hudson, S. R., Cohen, L., & Walden, V. (2015). *N-ICE2015 surface meteorology (Data set)*. Norwegian Polar Institute. https://doi.org/10.21334/npolar.2015.056a61d1

Hudson, S. R., Cohen, L., & Walden, V. P. (2016). *N-ICE2015 surface broadband radiation data (Data set)*. Norwegian Polar Institute. https://doi.org/10.21334/npolar.2016.a89cb766

Intrieri, J. M., Shupe, M. D., Uttal, T., & McCarty, B. J. (2002). An annual cycle of Arctic cloud characteristics observed by radar and lidar at SHEBA. *Journal of Geophysical Research*, *107*(C10), 8030. https://doi.org/10.1029/2000JC000423

Itkin, P., Spreen, G., Cheng, B., Doble, M., Girard-Ardhuin, F., Haapala, J., et al. (2017). Thin ice and storms: A case study of sea ice deformation from buoy arrays deployed during N-ICE2015. *Journal of Geophysical Research: Oceans*, *122*, 4661–4674. https://doi.org/10.1002/2016JC012403

Jin, Z., Charlock, T. P., Smith, W. L., Jr, & Rutledge, K. (2004). A look-up table for ocean surface albedo. *Geophysical Research Letters*, *31*, L2230.

Kato, S., Loeb, N. G., Rose, F. G., Doelling, D. R., Rutan, D. A., Caldwell, T. E., et al. (2013). Surface irradiances consistent with CERES-derived top-of-atmosphere shortwave and longwave irradiances. *Journal of Climate*, *26*, 2719–2740. https://doi.org/10.1175/JCLI-D-12-00436.1

Kato, S., Rose, F. G., Rutan, D. A., Thorsen, T. J., Loeb, N. G., Doelling, D. R., et al. (2018). Surface irradiances of Edition 4.0 clouds and the Earth's radiant energy system (CERES) energy balanced and filled (EBAF) data product. *Journal of Climate*, *31*, 4501–4527. https://doi.org/10.1175/JCLI-D-17-0523.1

Kay, J. E., L'Ecuyer, T., Chepfer, H., Loeb, N., Morrison, A., & Cesana, G. (2016). Recent advances in Arctic cloud and climate research. *Current Climate Change Reports*, *2*, 159. https://doi.org/10.1007/s40641-016-0051-9

Kay, J. E., & L'Ecuyer, T. (2013). Observational constraints on Arctic Ocean clouds and radiative fluxes during the early 21st century. *Journal of Geophysical Research: Atmospheres*, *118*, 7219–7236. https://doi.org/10.1002/jgrd.50489

Kayser, M., Maturilli, M., Graham, R. M., Hudson, S. R., Rinke, A., Cohen, L., et al. (2017). Vertical thermodynamic structure of the troposphere during the Norwegian young sea ICE expedition (N-ICE2015). *Journal of Geophysical Research: Atmosphere*, *122*(20), 10855–10872. https://doi.org/10.1002/2016JD026089

Key, J. (2002). *Streamer user's guide*. Cooperative Institute for Meteorological Satellite Studies, University of Wisconsin. http://stratus.ssec.wisc.edu/streamer/userman.pdf

Key, J., & Schweiger, A. J. (1998). Tools for atmospheric radiative transfer: Streamer and FluxNet. *Computers & Geosciences*, *24*(5), 443–451.

King, M. D., Platnick, S., Yang, P., Arnold, G. T., Gray, M. A., Riedi, J. C., et al. (2004). Remote sensing of liquid water and ice cloud optical thickness and effective radius in the arctic: Application of airborne multispectral MAS data. *Journal of Atmospheric and Oceanic Technology*, *21*, 857–875. https://doi.org/10.1175/1520-0426(2004)021<0857:RSOLWA>2.0.CO

Klett, J. D. (1985). Lidar inversion with variable backscatter/extinction ratios. *Applied Optics*, *24*, 1638–1643.

Lenaerts, J. T. M., Van Tricht, K., Lhermitte, S., & L'Ecuyer, T. S. (2017). Polar clouds and radiation in satellite observations, re-analyses, and climate models. *Geophysical Research Letters*, *44*, 3355–3364. https://doi.org/10.1002/2016GL072242

Liu, Y., & Key, J. R. (2016). Assessment of arctic cloud cover anomalies in atmospheric re-analysis products using satellite data. *Journal of Climate*, *29*(17), 6065–6083. https://doi.org/10.1175/JCLI-D-15-0861.1

Liu, Y., Shupe, M. D., Wang, Z., & Mace, G. (2017). Cloud vertical distribution from combined surface and space radar–lidar observations at two Arctic atmospheric observatories. *Atmospheric Chemistry and Physics*, *17*, 5973–5989. https://doi.org/10.5194/acp-17-5973-2017

Loeb, N. G., Doelling, D. R., Wang, H., Su, W., Nguyen, C., Corbett, J. G., et al. (2018). Clouds and the earth's radiant energy system (CERES) energy balanced and filled (EBAF) top-of-atmosphere (TOA) edition-4.0 data product. *Journal of Climate*, *31*(2), 895–918. https://doi.org/10.1175/JCLI-D-17-0208.1

Mariage, V., Pelon, J., Blouzon, F., Victori, S., Geyskens, N., Amarouche, N., et al. (2017). IAOOS microlidar-on-buoy development and first atmospheric observations obtained during 2014 and 2015 arctic drifts. *Optics Express*, *25*(4), A73–A84.

Martin, G. M., Johnson, D. W., & Spice, A. (1994). The measurement and parameterization of effective radius of droplets in warm stratocumulus. *Journal of the Atmospheric Sciences*, *51*, 1823–1842.

Minnis, P., Sun-Mack, S., Chen, Y., Chang, F.-L., Yost, C. R., Smith, W. L., Jr, et al. (2020). CERES MODIS cloud product retrievals for Edition 4, Part I: Algorithm changes. *IEEE Transaction on Geoscience and Remote Sensing*. 1–37. https://doi.org/10.1109/TGRS.2020.3008866

Minnis, P., Takano, Y., & Liou, K. N. (1993). Inference of cirrus cloud properties using satellite--observed visible and infrared radiances, Part I: Parameterization of radiance fields. *Journal of the Atmospheric Sciences*, *50*, 1279–1304.

Mitchell, D. L. (2002). Effective diameter in radiation transfer: General definition, applications, and limitations. *Journal of the Atmospheric Sciences*, *59*, 2330–2346.

Perovich, D. K., Grenfell, T. C., Light, B., & Hobbs, P. V. (2002). Seasonal evolution of the albedo of multiyear Arctic sea ice. *Journal of Geophysical Research*, *107*(C10), 8044. https://doi.org/10.1029/2000JC000438

Persson, P. O. G., Fairall, C. W., Andreas, E. L., Guest, P. S., & Perovich, D. K. (2002). Measurements near the Atmospheric Surface Flux Group tower at SHEBA: Near-surface conditions and surface energy budget. *Journal of Geophysical Research*, *107*(C10), 8045. https://doi.org/10.1029/2000JC000705

Pinnick, R. G., Jennings, S. G., Chýlek, P., Ham, C., & Grandy, W. T. (1983). Backscatter and extinction in water clouds. *Journal of Geophysical Research*, *88*(C11), 6787–6796. https://doi.org/10.1029/JC088iC11p06787

Pistone, K., Eisenman, I., & Ramanathan, V. (2014). Observational determination of albedo decrease caused by vanishing Arctic sea ice. *Proceedings of the National Academy of Sciences of the United States of America*, *111*(9), 3322–3326.

Pithan, F., Ackerman, A., Angevine, W. M., Hartung, K., Ickes, L., Kelley, M., et al. (2016). Select strengths and biases of models in representing the arctic winter boundary layer over sea ice: The larcform 1 single column model intercomparison. *Journal of Advances in Modeling Earth Systems*, *8*(3), 1345–1357. https://doi.org/10.1002/2016MS000630

Pithan, F., Svensson, G., Caballero, R., Chechin, D., Cronin, T. W., Ekman, A. M. L., et al. (2018). Role of air--mass transformations in exchange between the Arctic and mid--latitudes. *Nature Geoscience*, *11*, 805–812. https://doi.org/10.1038/s41561-018-0234-1

Provost, C., Pelon, J., Sennéchael, N., Calzas, M., Blouzon, F., Desautez, A., et al. (2015). IAOOS (Ice-Atmosphere-Arctic Ocean observing system, 2011-2019). *Mercator Ocean Quarterly Newsletter*, *51*, 13–15.

Rienecker, M. M., & Coauthors (2008). *The GOES-5 data assimilation system—documentation of Versions 5.0.1, 5.1.0, and 5.2.0*. NASA Tech. Rep. Series on Global Modeling and Data Assimilation NASA/TM-2008-104606, (Vol. 27, pp. 97). https://ntrs.nasa.gov/archive/nasa/casi.ntrs.nasa.gov/20120011955.pdf

Riihelä, A., Key, J. R., Meirink, J. F., Kuipers Munneke, P., Palo, T., & Karlsson, K.-G. (2017). An intercomparison and validation of satellite-based surface radiative energy flux estimates over the Arctic. *Journal of Geophysical Research: Atmospheres*, *122*, 4829–4848. https://doi.org/10.1002/2016JD026443

Rutan, D. A., Kato, S., Doelling, D. R., Rose, F. G., Nguyen, L. T., Caldwell, T. E., et al. (2015). CERES synoptic product: Methodology and validation of surface radiant flux. *Journal of Atmospheric and Oceanic Technology*, *32*, 1121–1143. https://doi.org/10.1175/JTECH-D-14-00165.1

Rutan, D., Rose, F., Roman, M., Manalo-Smith, N., Schaaf, C., & Charlock, T. (2009). Development and assessment of broadband surface albedo from Clouds and the Earth's Radiant Energy System clouds and radiation swath data product. *Journal of Geophysical Research*, *114*, D08125. https://doi.org/10.1029/2008JD010669

Sedlar, J. (2018). Spring arctic atmospheric preconditioning: Do not rule out shortwave radiation just yet. *Journal of Climate*, *31*, 4225–4240. https://doi.org/10.1175/JCLI-D-17-0710.1

Serreze, M. C., & Barry, R. G. (2011). Processes and impacts of arctic amplification: A research synthesis, global planet. *Change*, *77*, 85–96.

Shupe, M. D. (2011). Clouds at Arctic atmospheric observatories. Part II: Thermodynamic phase characteristics. *Journal of Applied Meteorology and Climatology*, *50*, 645–661. https://doi.org/10.1175/2010JAMC2468.1

Shupe, M. D., & Intrieri, J. M. (2004). Cloud radiative forcing of the Arctic surface: The influence of cloud properties, surface albedo, and solar zenith angle. *Journal of Climate*, *17*(13), 616–628. https://doi.org/10.1175/1520-0442(2004)017<0616:CRFOTA>2.0.CO;2

Shupe, M. D., Matrosov, S. Y., & Uttal, T. (2006). Arctic mixed-phase cloud properties derived from surface-based sensors at SHEBA. *Journal of the Atmospheric Sciences*, *63*, 697–711. https://doi.org/10.1175/JAS3659.1

Sotiropoulou, G., Tjernström, M., Sedlar, J., Achtert, P., Brooks, B. J., Brooks, I. M., et al. (2016). Arctic cloud summer experiment (ACSE): Boundary layer and cloud characteristics over ice and open-water, during the melt and freeze-up seasons. *Journal of Climate*, *29*, 8721–8744. https://doi.org/10.1175/JCLI-D-16-0211.1

Spinhirne, J. D., Boers, R., & Hart, W. (1989). Cloud top liquid water from lidar observations of marine stratocumulus. *Journal of Applied Meteorology and climate*, *28*, 81–90.

Spreen, G., Kaleschke, L., & Heygster, G. (2008). Sea ice remote sensing using AMSR-E 89 GHz channels. *Journal of Geophysical Research*, *113*, C02S03. https://doi.org/10.1029/2005JC003384

Stengel, M., Schlundt, C., Stapelberg, S., Sus, O., Eliasson, S., Willén, U., et al. (2018). Comparing ERA-Interim clouds with satellite observations using a simplified satellite simulator. *Atmospheric Chemistry and Physics*, *18*, 17601–17614. https://doi.org/10.5194/acp-18-17601-2018

Stephens, G. L. (1978). Radiation profiles in extended water clouds: II. Parameterization schemes. *Journal of the Atmospheric Sciences*, *35*, 2123–2132.

Stephens, G., Winker, D., Pelon, J., Trepte, C., Vane, D., Yuhas, C., et al. (2018). CloudSat and CALIPSO within the A-Train: Ten years of actively observing the Earth system. *Bulletin of the American Meteorological Society*, *99*, 569–581. https://doi.org/10.1175/BAMS-D-16-0324.1

Stramler, K., Del Genio, A. D., & Rossow, W. B. (2011). Synoptically driven Arctic winter states. *Journal of Climate*, *24*(6), 1747–1762. https://doi.org/10.1175/2010JCLI3817.1

Taylor, J. P., Edwards, J. M., Glew, M. D., Hignett, P., & Slingo, A. (1996). Studies with a flexible new radiation code. II: Comparisons with aircraft short-wave observations. *Quarterly Journal of the Royal Meteorological Society*, *122*, 839–861. https://doi.org/10.1002/qj.49712253204

Tjernström, M., Leck, C., Birch, C. E., Bottenheim, J. W., Brooks, B. J., Brooks, et al. (2014). The arctic summer Cloud Ocean study (ASCOS): Overview and experimental design. *Atmospheric Chemistry and Physics*, *14*, 2823–2869. https://doi.org/10.5194/acp-14-2823-2014

Turner, D. D. (2005). Arctic mixed-phase cloud properties from AERI lidar observations: Algorithm and results from SHEBA. *Journal of Applied Meteorology*, *44*, 427–444. https://doi.org/10.1175/JAM2208.1

Uttal, T., & co-authors (2016). International arctic systems for observing the atmosphere: An international polar year legacy consortium. *Bulletin of the American Meteorological Society*, *97*(6), 1033–1056. https://doi.org/10.1175/BAMS-D-14-00145.1

Van Tricht, K., Lhermitte, S., Gorodetskaya, I. V., & van Lipzig, N. P. M. (2016). Improving satellite-retrieved surface radiative fluxes in polar regions using a smart sampling approach. *The Cryosphere*, *10*, 2379–2397. https://doi.org/10.5194/tc-10-2379-2016

Vaughan, M.A., Garnier, A., Tackett, J. L., Avery, M. A., Kar, J., Liu, Z., et al. (2017). *Overview of the CALIPSO version 4 lidar data products*. 8th Symposium on Lidar Atmospheric Applications, 97th Annual Meeting. Seattle, WA: American Meteorological Society.

Vihma, T., Jaagus, J., Jakobson, E., & Palo, T. (2008). Meteorological conditions in the Arctic Ocean in spring and summer 2007 as recorded on the drifting ice station Tara. *Geophysical Research Letters*, *35*, L18706. https://doi.org/10.1029/2008GL034681

Walden, V. P., Hudson, S. R., Cohen, L., Murphy, S. Y., & Granskog, M. A. (2017). Atmospheric components of the surface energy budget over young sea ice: Results from the N-ICE2015 campaign. *Journal of Geophysical Research: Atmospheres*, *122*, 8427–8446. https://doi.org/10.1002/2016JD026091

Wang, C., Graham, R. M., Wang, K., Gerland, S., & Granskog, M. A. (2019). Comparison of ERA5 and ERA-Interim near-surface air temperature, snowfall and precipitation over Arctic sea ice: effects on sea ice thermodynamics and evolution. *The Cryosphere*, *13*(6), 1661–1679. https://doi.org/10.5194/tc-13-1661-2019

Wang, C., Graham, R. M., Wang, K., Gerland, S., & Granskog, M. A. (2019). Comparison of ERA5 and ERA-Interim near-surface air temperature, snowfall and precipitation over Arctic sea ice: Effects on Sea ice thermodynamics and evolution. *The Cryosphere*, *13*(6), 1661–1679. https://doi.org/10.5194/tc-13-1661-2019

Winker, D. M., Vaughan, M. A., Omar, A., Hu, Y., & Powell, J. A. (2009). Overview of the CALIPSO mission and CALIOP data processing algorithms. *Journal of Atmospheric and Oceanic Technology*, *26*, 2310–2323. https://doi.org/10.1175/2009JTECHA1281.1

Wiscombe, W. J., & Warren, S. G. (1980). A model for the spectral albedo of snow. I: Pure snow. *Journal of the Atmospheric Sciences*, *37*, 2712–2733. https://doi.org/10.1175/1520-0469(1980)037<2712:AMFTSA>2.0.CO;2

Zygmuntowska, M., Mauritsen, T., Quaas, J., & Kaleschke, L. (2012). Arctic Clouds and Surface Radiation-A critical comparison of satellite retrievals and the ERA-Interim re-analysis. *Atmospheric Chemistry and Physics*, *12*, 6667–6677. https://doi.org/10.5194/acp-12-6667-2012

References From the Supporting Information

Garnier, A., Pelon, J., Dubuisson, P., Yang, P., Faivre, M., Chomette, O., et al. (2013). Retrieval of cloud properties using CALIPSO Imaging Infrared Radiometer. Part II: Effective diameter and ice water path. *Journal Applied Meteorology Climatology*, *52*, 2582–2599. https://doi.org/10.1175/JAMC-D-12-0328.1

Khanal, S., & Wang, Z. (2018). Uncertainties in MODIS-based cloud liquid water path retrievals at high latitudes due to mixed-phase clouds and cloud top height inhomogeneity. *Journal of Geophysical Research: Atmosphere*, *123*, 11154–11172. https://doi.org/10.1029/2018JD028558

Platnick, S., Meyer, K., King, M. D., Wind, G., Amarasinghe, N., Marchant, B., et al. (2017). The MODIS cloud optical and microphysical products: Collection 6 updates and examples from Terra and Aqua. *IEEE Transactions on Geoscience and Remote Sensing*, *55*, 502–525. https://doi.org/10.1109/TGRS.2016.2610522